Friction-Induced Vibrations in Railway Transportation

by

Chandra Prakash Sharma

B. Tech., Sardar Vallabhbhai National Institute of Technology, India, 2007

A THESIS SUBMITTED IN PARTIAL FULFILLMENT
OF THE REQUIREMENTS FOR THE DEGREE OF

MASTER OF APPLIED SCIENCE

in

THE FACULTY OF GRADUATE STUDIES
(Mechanical Engineering)

The University Of British Columbia
(Vancouver)

November 2011

Abstract

Controlling friction at the wheel-rail interface is indispensable for extending track life, minimising wheel-flange wear, improving fuel efficiency, reducing noise and lateral forces. A particular implementation of friction modifier system consists of a stick-tube assembly, attached through a bracket which is suspended from the railway bogie frame. Inside the tube, a set of interlocking solid sticks resides with one end pressed against the tread or flange of the wheel, and the other end against a constant force tape spring. Rubbing action at the stick-wheel interface and the action of the spring results in a gradual transfer of friction modifier film to the wheel and thence to the rail through the wheel-rail contact. This results in effective friction management between the wheel and the rail. Friction modifier systems can experience unstable friction-induced vibrations due to a complex set of *in situ* contact conditions. Stability prediction is important for efficient functioning of friction control systems. This dissertation contributes a stability analysis procedure in frequency domain based on Frequency Response Functions (FRFs) of the wheel and the applicator-bracket subsystems. The stability analysis yields stability maps delineating stable and unstable regions of operation in the design parameter space defined by speed of train, angle of applicator, and friction coefficient. Stability characteristics of three bracket designs are compared using experiments and finite element models. Results are summarised in the form of stability diagrams indicating the operating conditions that will lead to unstable vibrations. This methodology can easily incorporate design changes to the bracket and/or applicator, thus facilitating a rapid comparison of different designs for their stability characteristics even before they are built.

Table of Contents

Abstract . . . . . **ii**

Table of Contents . . . . . **iii**

List of Tables . . . . . **vi**

List of Figures . . . . . **vii**

Glossary . . . . . **x**

Acknowledgments . . . . . **xi**

Dedication . . . . . **xii**

1 Introduction **1**

1.1 Friction Control Systems 2

1.2 Solid Stick Technology 4

2 Literature Review **8**

2.1 Introduction 8

2.2 Friction in Engineering 9

2.2.1 Friction Models 9

2.2.2 Friction Management in Railways 10

2.3 Friction-Induced Vibration Phenomena 16

2.3.1 Disk Brake Squeal 18

2.3.2 Railway Noise 20

2.3.3 Curve Squeal . . . 22
2.4 Vibrations of Rotating Disks . . . 24
2.5 Conclusions . . . 26
2.6 Scope and Outline . . . 28

3 Stability Analysis . . . 30
3.1 Introduction . . . 30
3.2 Design Parameters . . . 31
3.3 Modelling in Frequency Domain . . . 34
3.3.1 Frequency Domain Stability Analysis . . . 36
3.3.2 Control Theory Background . . . 38
3.4 Stability Prediction Methodology . . . 41
3.5 Conclusion . . . 43

4 Experiments and Modelling . . . 45
4.1 Introduction . . . 45
4.2 Experiments . . . 46
4.2.1 Full Wheel Test Rig . . . 46
4.2.2 Impulse Tests . . . 48
4.2.3 Operational Tests . . . 55
4.2.4 Summary of Measurements . . . 56
4.3 Finite Element Modelling . . . 57
4.3.1 Wheel FE Model . . . 57
4.3.2 Applicator-bracket FE Models . . . 60
4.3.3 Proportional Damping Model . . . 63
4.3.4 Summary of FE Modelling . . . 64
4.4 Validation of FE Models by Experiments . . . 65
4.5 Conclusion . . . 66

5 Influence of Bracket Designs on Stability . . . 68
5.1 Introduction . . . 68
5.2 Influence of Train Speed and Angle of Applicator . . . 69
5.2.1 Influence of Wheel Rotation: Mode Splitting . . . 69
5.2.2 Orientation of Applicator . . . 73

5.3 Stability Diagrams 74
5.4 Comparison of Bracket Designs 79
5.5 Conclusion 80

6 Conclusions 82
6.1 Contribution of This Dissertation 83
6.2 Suggestions for Further Research 83

Bibliography 85

List of Tables

Table 4.1 Summary of experimentally obtained natural frequencies . . . 57
Table 4.2 Material properties for the railway wheel. 58
Table 4.3 Modelling parameters for applicator-bracket assembly. 62
Table 4.4 Bracket Design-B: Analysis of FRF data for modal parameters 63
Table 4.5 Experimentally determined modal damping parameters α and β 64
Table 4.6 Summary of FE obtained natural frequencies 65
Table 4.7 Validation of FE model predictions for natural frequencies in Hz with experimental values 66

List of Figures

Figure 1.1 Liquid Top Of Rail (TOR) friction modification system 2
Figure 1.2 Friction modification systems 3
Figure 1.3 Low Coefficient of Friction (LCF) solid stick friction control system for application on the wheel flange. 4
Figure 1.4 Flange lubricating device originally conceived and patented by Dawson. 5
Figure 1.5 Bracket designs 7

Figure 2.1 Friction models. 11
Figure 2.2 The generalized Stribeck curve 12
Figure 2.3 Relationship between traction and creep. 13
Figure 2.4 Behaviour of friction modifiers. 14
Figure 2.5 Frictional characteristics of different friction management products, LCF, HPF and VHPF. 15
Figure 2.6 Three-dimensional plots of the (μ,s,v) curves measured on a car tyre. 16
Figure 2.7 Pin-on-disk model of a disk brake. 19
Figure 2.8 A model of the cantilever-disc system. 20
Figure 2.9 Generation of lateral creepage by a non-zero yaw angle 23
Figure 2.10 A typical frequency speed diagram. 27
Figure 2.11 Wheel-applicator-bracket system. 28
Figure 2.12 A pictorial overview of this dissertation. 29

Figure 3.1 Plan view of the friction control system depicting angle of applicator, α for a particular applicator/bracket mounting configuration, which is parallel to plane of the ground 31
Figure 3.2 Applicator-wheel contact model 33
Figure 3.3 Schematic diagram of applicator-wheel coupled system indicating interacting forces and displacements at the contact point. 35
Figure 3.4 Block diagram of stability criterion 38
Figure 3.5 Stability regions in s-domain 39
Figure 3.6 Stability regions in Laplace and Fourier planes 41
Figure 3.7 Flowchart for stability prediction methodology 43

Figure 4.1 Bracket designs 46
Figure 4.2 Full Wheel Test Rig 47
Figure 4.3 A schematic of the signal flow in experimental modal analysis 48
Figure 4.4 Co-ordinate directions represented by tri-axial accelerometer . 49
Figure 4.5 Experimental setup 50
Figure 4.6 A typical time history data obtained by data acquisition system 52
Figure 4.7 A typical frequency response data of Bracket Design-A. . . . 52
Figure 4.8 A typical frequency response data for one channel with coherence function 53
Figure 4.9 FRF for Bracket Design-A 54
Figure 4.10 FRF for Bracket Design-B 54
Figure 4.11 FRF for Bracket Design-C 55
Figure 4.12 Impulse response spectrum for the wheel 55
Figure 4.13 Running wheel test 56
Figure 4.14 FE analysis of railway wheel 58
Figure 4.15 Wheel mode-shapes produced by ABAQUS 59
Figure 4.16 FE model of applicator with bracket 60
Figure 4.17 FE model of applicator with bracket mounted on a frame . . . 61
Figure 4.18 FE model of applicator with bracket on the supporting I-beam (rail) 61
Figure 4.19 Proportional damping model fit $2\zeta_n = \frac{\alpha}{\omega_n} + \beta\omega_n$ for the Bracket Design-B. 64

Figure 5.1 Summary of Frequency Response Function matrix, $\boldsymbol{H}$, for Bracket Design – A in the frequency range $0-600$ Hz 70
Figure 5.2 Summary of Frequency Response Function matrix, $\boldsymbol{H}$, for Bracket Design – B in the frequency range $0-600$ Hz 70
Figure 5.3 Summary of Frequency Response Function matrix, $\boldsymbol{H}$, for Bracket Design – C in the frequency range $0-600$ Hz 71
Figure 5.4 Summary of Frequency Response Function matrix, $\boldsymbol{G}$, for railway wheel in the frequency range $0-2000$ Hz 71
Figure 5.5 Split mode-shapes owing to wheel rotation, corresponding to the train speed of 16 km/h 73
Figure 5.6 The plot shows poles and zeros for individual transfer functions for a typical case 75
Figure 5.7 Plot shows a typical unstable system, wherein the zeros indicated as dark circles are also present in the lower half of the complex plane, indicating instability 76
Figure 5.8 Stability diagram for Bracket Design–A: angle of applicator versus coefficient of friction for different train speeds 77
Figure 5.9 Stability diagram for Bracket Design–A: angle of applicator versus train speed 78
Figure 5.10 Stability diagram for Bracket Design–A: coefficient of friction versus train speed 79
Figure 5.11 Stability diagram for Bracket Design–A: angle of applicator versus coefficient of friction at several train speeds 80
Figure 5.12 Stability diagram for Bracket Design–B: angle of applicator versus coefficient of friction for different train speeds 80
Figure 5.13 Stability diagram for Bracket Design–C: angle of applicator versus coefficient of friction for different train speeds 81

Glossary

Abbreviations

TOR	Top-Of-Rail
FCS	Friction Control System
LCF	Low Coefficient of Friction
LCF-AR	Low Coefficient of Friction-Abrasion Resistant
HPF	High Positive Friction
FWTR	Full Wheel Test Rig
FRF	Frequency Response Function
FE	Finite Element
CLTF	Closed Loop Transfer Function
FFT	Fast Fourier Transform
CAD	Computer Aided Design
RFP	Rational Fraction Polynomial
TF	Transfer Function

Symbols

$\boldsymbol{G}$	Wheel Transfer Functions
$\boldsymbol{H}$	Applicator Transfer Functions
N	Normal Force
N_o	Steady Component of Normal Force
N'	Fluctuating Component of Normal Force
F	Friction Force
F_o	Steady Component of Friction Force
F'	Fluctuating Component of Friction Force
μ	Coefficient of Friction
α	Angle of Applicator
v	Speed of Train

The words transfer function (TF) and frequency response function (FRF) are used interchangeably.

Acknowledgments

I would like to express my gratitude to my supervisor, Dr. A. Srikantha Phani for his support and encouragement throughout the project. I thank my colleagues for healthy discussions and creating a congenial research atmosphere in the Dynamic and Applied Mechanics Laboratory (DAL). They have always been a constant source of ideas, creative energy and enthusiasm.

Financial support from Natural Sciences and Engineering Research Council and Kelsan Technologies Corp. is thankfully acknowledged. I would like to thank Dr. Donald T Eadie and Mr. Ron Hui from Kelsan Technologies Corp. for their technical inputs, advise and making available shop and test facilities.

This dissertation is dedicated to my wonderful parents, Kiran Sharma and Satya Prakash Sharma, for all they have done for me. I would like to express my heartfelt gratitude to my aunt Hemlata Sharma and uncle Yatendra Sharma for providing a homely atmosphere and giving me all the support in the world to complete this work.

To My Parents

Chapter 1

Introduction

Rail transport is one of the most economic and widely used means of conveyance for passengers and goods. Friction existing between the rail and wheel has been a cause of concern for decades resulting in wheel flange/rail wear and generation of excessive noise especially around the curves. Faced with stiff market pressures and higher volume of transport, trains are becoming heavier [1] resulting in increased axle loads and lateral forces on tracks. Minimizing wear and fuel consumption remains a challenge for railroad engineers.

Friction control in transportation systems can lead to many environmental benefits such as reduction in unwanted sound and vibration, and economical benefits such as extending the life of railway wheels and track. Controlling friction at the wheel-rail interface can lead to significant reduction in wear and thereby decrease the operating costs involved in maintaining a railway track.

Earlier, railway industry had to rely on traditional lubricants such as oil and grease in order to keep a check on wear rates. After years of research in the field of rail and wheel tribology, it has been established that there is a selective requirement of choice of coefficient of friction for Top Of Rail (TOR) and on the sides. In practice, top of rail should not have too low a coefficient of friction as it would cause braking and traction problems. From the tribological studies, an optimum value for coefficient of friction for TOR application was found to be around 0.35 [2]. But for the wheel flange/gauge face of the rail, the friction coefficient should be less than 0.2. Traditional forms of lubricants applied on the gauge of the rail fail to fulfil

these criteria. And in most cases, the lubricant gets transferred to top of rail causing undesirable braking and traction problems. Moreover, they are very difficult to maintain and lead to contamination of railroad bed as they easily coalesce with surrounding dirt. Fire remains a potential hazard making the traditional lubricants for friction control limited in terms of their application, control and reliability.

1.1 Friction Control Systems

(a) TOR distribution bars **(b)** Trackside reservoir tank

Figure 1.1: Liquid Top Of Rail (TOR) friction modification system

Recent advancements in friction control technology led to the development of much more sophisticated friction modification systems. Use of these friction modifiers significantly reduces the curving forces, flange noises and corrugations thus extending track and wheel life. Modern day transit and freight trains are equipped with several reliable on-board and trackside lubrication systems as described below.

1. **Liquid Top-Of-Rail (TOR) Friction Modification System** - It uses water based liquid friction modifiers applied using a trackside Top-of-Rail application system. See Figure 1.1. This trackside system is equipped with a product reservoir tank/control unit, top of rail distribution bars and associated connecting tubes to regulate the flow of friction modifier. The liquid friction

modifier is applied directly on the Top-of-Rail and is subsequently picked up by the train wheels and carried down the track. Water evaporates leaving a dry thin film on the rail-wheel interface providing an effective friction control. It is intended for use in targeted curve locations in transit systems and efficiently reduces wheel squeal noise, short pitch corrugations, and lateral forces.

2. **HiRail Vehicle mounted TOR Friction Control System**- The application system, see Figure 1.2a, is mounted on a Hi-Rail truck which evenly sprays the water based liquid friction modifier on top of rail as it drives along the track. This develops a thin film on the rail surface which is also transferred to the wheels as they pass over the rails. This provides the necessary friction control at the interface.

(a) HiRail Vehicle mounted TOR Friction Control System

(b) Liquid LCF Gauge Face Lubricant

Figure 1.2: Friction modification systems

3. **Spray based Top-Of-Rail Friction liquid friction modifiers**- This on-board friction control system is designed to spray water based liquid friction modifier on the top of rail throughout the railway track. It optimizes the coefficient of friction on the wheel/rail interface to the desired value.

4. **Liquid LCF (Low Coefficient of Friction) Gauge Face Lubricant**- This

system, shown in 1.2b, is a manual application method particularly useful for short sections of the track with sharp curves. The LCF lubricant is applied to the gauge face of the rail through a special applicator, which works like a paint roller as it applies the liquid to the gauge face. It mitigates rail gauge wear at specific locations.

An alternate to aforementioned friction control systems is a solid stick based friction modifier as shown in Figure 1.3 which will be discussed next.

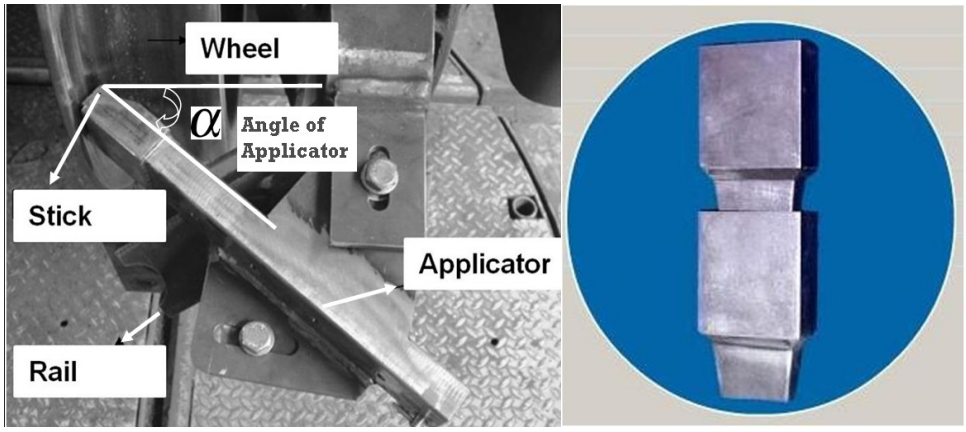

(a) Applicator Wheel Assembly **(b)** LCF Interlocking Sticks

Figure 1.3: Low Coefficient of Friction (LCF) solid stick friction control system for application on the wheel flange.

1.2 Solid Stick Technology

One of the cheapest and efficient ways to control friction at the wheel flange and inner face of the rail interface is the vehicle mounted solid stick lubrication system. The idea of Solid Stick Technology was first introduced by Dawson [3] who filed a patent on ***Flange Lubricating device*** in 1911. See Figure 1.4 for the spring loaded design mechanism of the lubricating device. Kelsan Technologies developed their solid friction modifier in early 1990s with ***Vancouver Sky Train*** transit system as one of their first customers. Later on, advanced forms of liquid based friction modifier systems were also developed. However, Solid Stick Technology always

found the edge due to ease of installation and maintenance, fire safety and other significant operating benefits such as self-regulated transfer of friction modifier material.

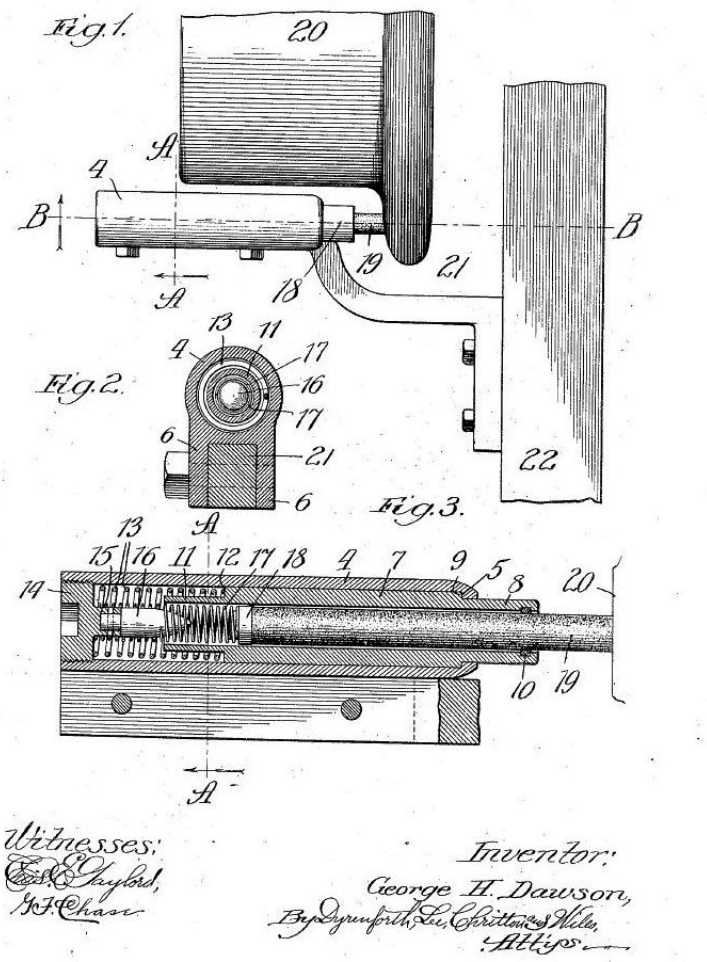

Figure 1.4: Flange lubricating device originally conceived and patented by Dawson [3]

A solid stick lubricant is placed in a hollow tube called Applicator and is applied directly to the wheel flange of transit vehicle via a spring loaded mechanism. The bracket/applicator assembly is attached to the frame of the transit vehicle as shown in Figure 1.3a. The solid sticks, see Figure 1.3b, are primarily comprised of

solid lubricant in a thermosetting polymer matrix. The solid lubricant transfers to the wheel flange of the transit vehicle, and the polymer evaporates off due to high temperatures at the flange / rail interface. Finally a thin dry solid lubricant film on the flange provides a low coefficient of friction. The film also transfers to the side of the rail, and from there to the non-applied wheel flanges as well. So a '*third body*' thin film of lubricant is left behind on the gauge face of the rail that provides supreme lubrication to the rail/wheel interface throughout the railway system.

The solid stick lubrication provides a controlled coefficient of friction by modifying the existing friction conditions between the rail and the wheel to the required level. With time, solid stick lubricants gained prominence as opposed to the conventional lubricants for their greater degree of control on achieving the target friction levels. They ensure cleanliness and can work efficiently in conjunction with traditional lubricants as well. Solid Sticks are interlocking in nature, easy to refill and residue left on the track is non-toxic. Typical wear rates of solid sticks range from 1000-2000 miles/inch (expressed in distance travelled by the train per unit length of the stick consumed) depending upon the track conditions and the type of stick used. They are non-flammable in nature which ensures fire safety particularly for underground metro systems, where oil and grease can pose a significant fire hazard. Furthermore, solid sticks are custom designed and are available in different shapes and composition. They can be straight or curved depending on the space constraints for application. Commonly available sticks are described below.

1. **LCF** (**L**ow **C**oefficient of **F**riction)- It is a dry solid lubricant, essentially a polymetric matrix with no oil or liquid components. It is best suited for high pressures at the wheel/rail interface. This ensures a low coefficient of friction (0.1-0.2) at wheel flange without any migration to the wheel tread or railhead.

2. **LCF-AR**- This has an additional advantage of being more Abrasion Resistant (AR). This is critical where abrasive effect due to track conditions, wheel metallurgy or harsh environment can escalate the stick consumption.

3. **HPF** (**H**igh **P**ositive **F**riction)- Solid stick technology is also used for controlling Top-of-Rail (TOR) friction by the use of HPF modifiers. These HPF

sticks are directly applied onto the wheel tread of the transit vehicle, thereby providing a consistent friction level of about 0.35 at the wheel/rail interface. HPF can be utilized alone or in dual application with LCF for a complete friction management solution.

Owing to significant benefits over its counterparts, solid lubrication is now widely used in freight, heavy haul locomotives, transit and high speed trains [4]. Applicator-stick systems are applied on the wheels using custom designed brackets for the railway bogie. Three bracket designs used in different transit systems are chosen in this study. They are as shown in Figure 1.5.

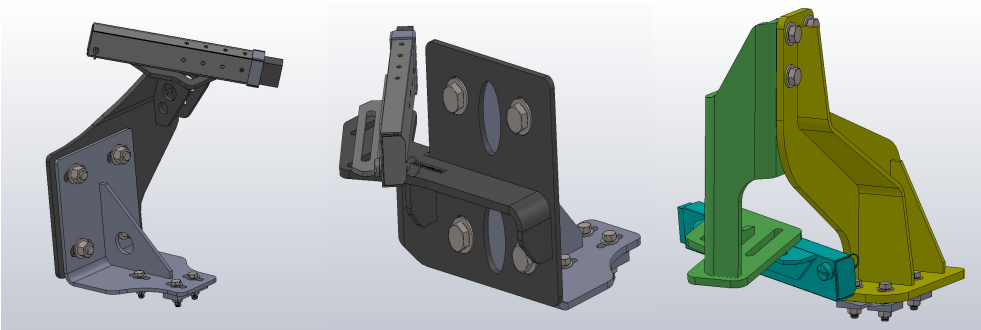

(a) Bracket Design-A **(b)** Bracket Design-B **(c)** Bracket Design-C

Figure 1.5: Bracket designs

Excessive vibration and noise due to friction induced instabilities is a potential problem associated with solid stick friction control systems. This can result in improper application of the lubricant, stick chatter and squeal. Given the significant benefits obtained through friction control, it is necessary to develop stability comparison tools for different designs. This forms the main theme of this dissertation.

Chapter 2

Literature Review

2.1 Introduction

Friction related phenomena occur in everyday life (squealing shoes, screeching doors) and they severely restrict the performance of many engineered systems ranging from disc brakes in automotive industry to wheel-rail noise in railway transportation. In musical acoustics, however, they are desired. For example, in Violin, rosin is applied on to the bow to alter the coefficient of friction between the bow and the string and produce pleasant music. It is not surprising that the study of friction and associated vibrations is very broad.

In this chapter, literature pertaining to friction in general and friction management in Railway systems in particular is surveyed first in Section 2.2. Friction-Induced vibration phenomena in engineering applications is considered next in Section 2.3.

The need for friction modifiers and typical friction modification systems have already been introduced in Chapter 1. An overview of friction at wheel-rail contact and necessary tribological background relevant to Railway transportation is given in Section 2.2.2. After a brief overview of wheel-rail contact mechanics this section brings forth the need for friction management to reduce wear and noise in Railway systems. Friction-Induced vibration phenomena in automotive and railway industries are surveyed in Section 2.3 with particular emphasis on self-excited vibrations originating from a contact between two mechanical systems. Specifically, litera-

ture on squeal noise in disc brake systems and railway noise around curves due to stick-slip oscillations is surveyed.

A brief review of literature on vibrations of rotating discs is presented in Section 2.4. This is needed to understand the dynamics of the railway wheel in motion.

This chapter concludes with an outline of the scope of this dissertation and identifies appropriate methodologies from literature to model friction-induced vibrations in solid stick friction modifier systems.

2.2 Friction in Engineering

2.2.1 Friction Models

Friction is a very complex phenomenon. It is a multi-valued non-linear process [5] with respect to the relative sliding speed, random process with respect to time and non-linear for higher normal load. Friction is dependent on the material properties, roughness and geometry of the sliding surfaces and even temperature plays a significant role. Besides, contact mechanics of interacting surfaces e.g., the physics for metal-metal contact or a polymer-metal contact is completely different. Friction induced dynamic instabilities—often associated with a negative slope of the friction characteristic curve —such as chatter and squeal can arise due to a complex set of *in situ* contact conditions, normal contact pressure and temperature. They are notorious for their twitchiness and unpredictability [6].

Several mechanisms ranging from microscopic asperitites to presence of contaminants, fluctuations in temperature and normal forces can alter friction at the interface between two surfaces in contact. The friction force F is related to normal force N via $F = \mu N$, where μ is coefficient of friction. For static problems there is no relative velocity at the point of contact, however once relative motion takes place the coefficient of friction drops to a kinetic value (μ_k) which is usually lower than the static friction coefficient (μ_s). Commonly used friction models in engineering are phenomenological. The three widely used models are viscous, Coulomb, Stribeck type as shown in Figure 2.1. Many other models exist too and they are surveyed in [5, 7]. In a viscous model, the variation with respect to velocity is linear. In a Coulomb model the static friction coefficient associated with zero

relative velocity is indeterminate. Stribeck model allows for the continuous drop of the friction coefficient from the static to kinetic value at low velocities and can be viewed as a combination of negative viscous for low velocities, and a combination of Coulomb and Viscous models for higher velocities. Many approaches to study friction from contact mechanics to continuum mechanics exist. The relevance of different approaches to friction modelling is summarised in Figure 2.2. This graph highlights that for high velocities, high viscosities and low normal loads continuum mechanics approaches are adequate. However, for high normal forces contact mechanics is more appropriate. In Railway systems, the normal force is exceedingly large and hence contact mechanics play a critical role. The introduction of a "third body" friction modifier layer between the wheel and the rail surfaces can alter the contact forces significantly.

2.2.2 Friction Management in Railways

In the railway vehicle dynamics, friction is responsible for the wheel-rail wear, rolling contact fatigue, short pitch corrugations and associated noise generation mechanisms. It is important to recognise that both friction and wear are system parameters and not material parameters. Wear in general, occurs when two surfaces move relative to each other under some load. Thus, contact conditions play a deciding role on wear-rates. Therefore the study of friction, wear and lubrication is essentially an interdisciplinary subject and this interdependence highlights the need for study of tribology of rail-wheel contact.

Wheels and rail are deformable, especially in the contact zone where the normal forces are severely high. The wheel and rail conform to each other over a region of contact with some distortion always taking place at the point of contact. Typically, such an area of contact is elliptical in shape assuming Hertzian contact law to be valid. This distortion is localized and small and thus gives rise to large forces. Besides, when any acceleration or braking takes place or when the vehicle is subjected to lateral forces during curving, rail-wheel contact zone distorts. The tangential forces create a portion of distortion where they first come in contact, followed by a region of slippage at the trailing edge. Consequently, pure rolling motion seldom takes place. This makes the wheel not to advance as far as one

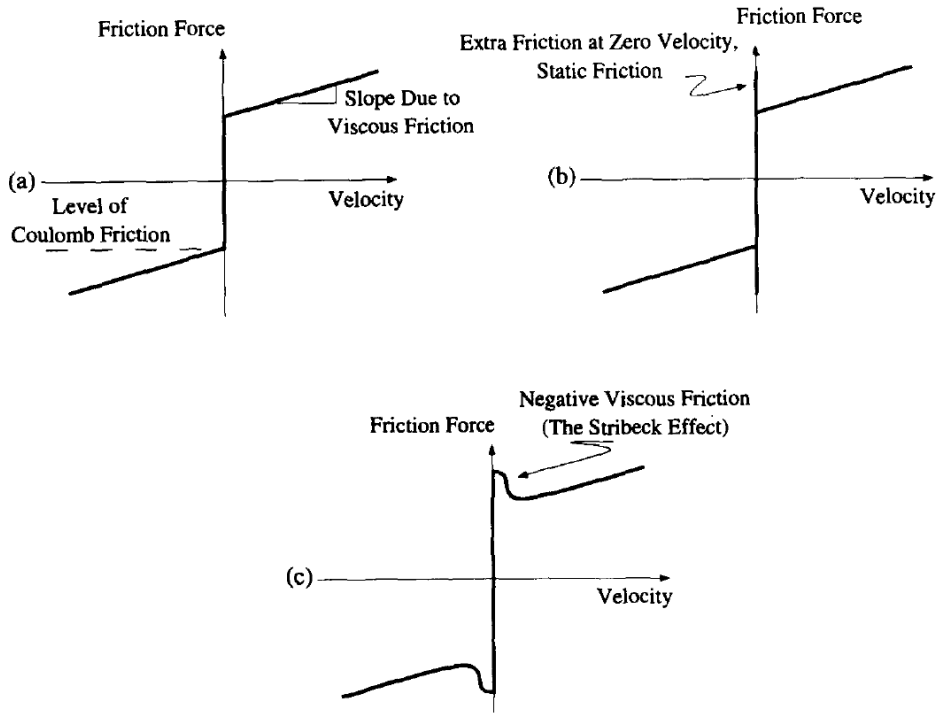

Figure 2.1: Friction models: (a): Coulomb + viscous friction model; (b): static + Coulomb + viscous friction model; (c): negative viscous + Coulomb + viscous friction model (Stribeck friction) [7]

would expect from pure rolling considerations during traction. Conversely, the same contact distortions mean that it advances farther during braking. This combination of elastic distortion and local slipping is known as creep. Mathematically it can be represented as [9, 10]:

$$\text{Longitudinal creep} = \frac{\text{actual forward displacement} - \text{pure rolling forward displacement}}{\text{forward displacement due to rolling}}. \tag{2.1}$$

Note that lateral and spin creepages do exist and can be defined similarly. It is a common practise in Railway literature to plot the variation of traction force μN as a function of creep. One such plot is shown in Figure 2.3.

For small longitudinal creepages, the traction forces are directly proportional to the corresponding creepages [12]. With the increase in tractive force, the stick

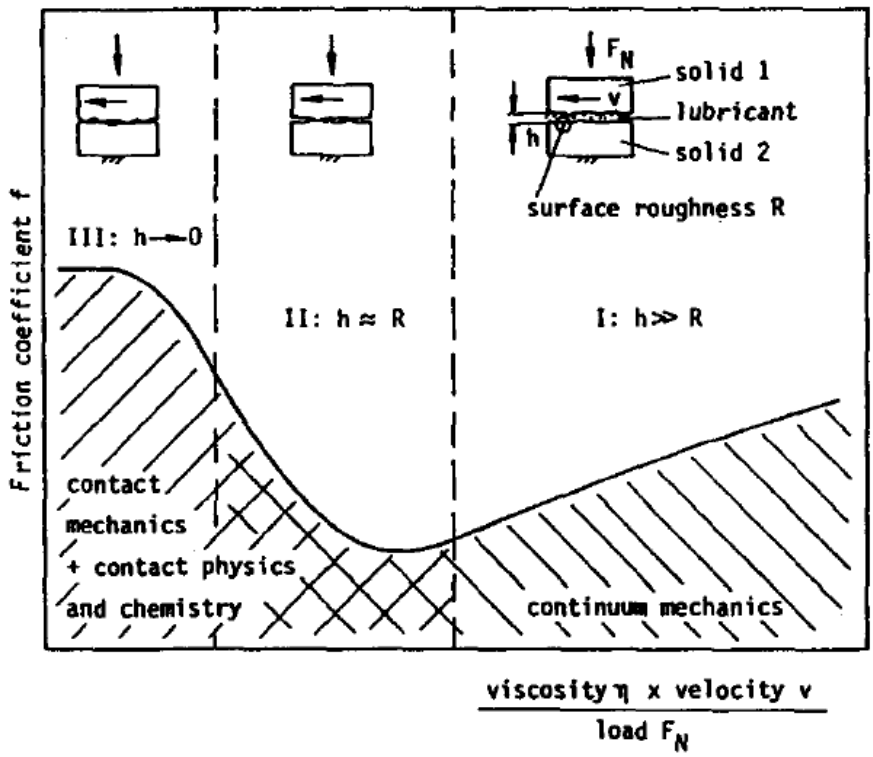

Figure 2.2: The Generalized Stribeck Curve [8].

region decreases and slip region increases, effectively leading to a rolling-sliding contact. A saturation level for traction force occurs when the stick region completely disappears and the entire contact patch is in a state of pure sliding. This is the maximum traction force one can get, and it depends on the capability of the contact area to absorb traction. In practice, maximum wheel-rail traction is obtained at creep levels of 0.01 to 0.02. Beyond this maximum wheel-rail traction the traction vs. creep curve might fall as shown in Figure 2.4. This gives rise to a negative friction characteristic which leads to a phenomenon of roll-slip oscillations (stick-slip) of the wheel-rail traction force. Roll-slip oscillations [13] are responsible for rail-wheel corrugations and associated high pitched squeal noise, particularly on track conditions with high level of friction and negative friction characteristics.

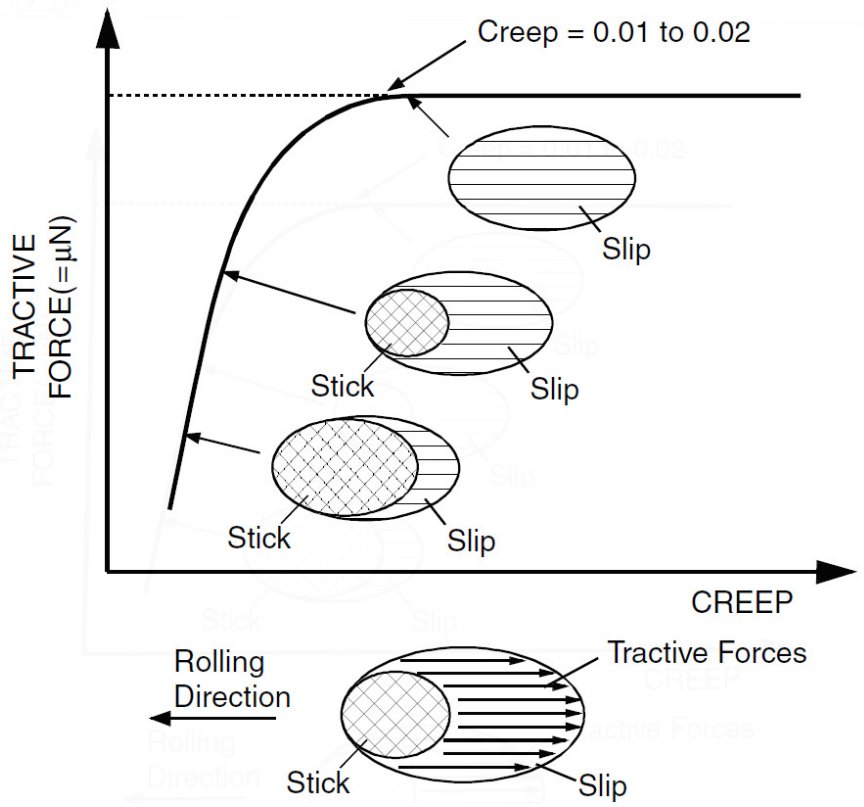

Figure 2.3: Relationship between traction and creep in the wheel-rail contact [11].

Introduction of a 'third body' layer between the rail and wheel surface can dramatically change the rheological parameters of the contact and in turn change the traction-creep curve. Thus, by introducing friction modifier material at the rail-wheel interface, one can achieve target friction levels and overcome the negative friction characteristics and prevent stick-slip, wheel noise and curve squeal.

It is a widely accepted fact that negative friction is responsible for the occurrence of stick-slip phenomenon, which in turn results in excessive noise and rail-wheel wear. Therefore, it is necessary to understand the concepts of negative and positive friction. In the context of creep, positive friction implies that the coefficient of friction increases with creep. Conversely for negative friction, coefficient of friction decreases with creep. Friction management strategy aims at changing

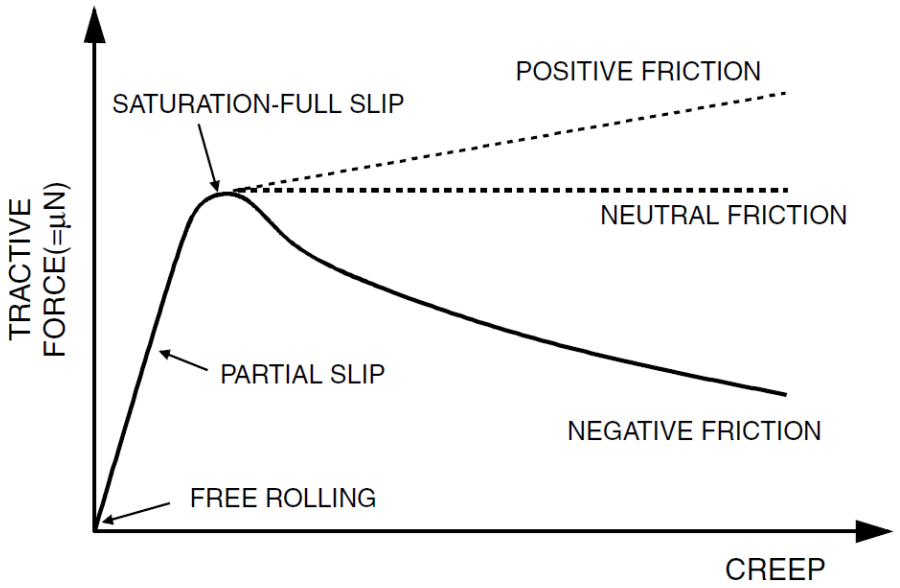

Figure 2.4: Behaviour of friction modifiers [11].

the existing negative friction conditions to a positive one by introducing a layer of friction modifier between rail and wheel. This is the central idea behind many friction management strategies [2] employed in railways. Figure 2.5 shows the friction characteristics of commercially available friction modifiers. The selective friction control strategy aims to achieve the following.

- Low friction at the wheel flange-rail gauge contact, to reduce wear and flange noises especially at the curves.
- Intermediate friction at the wheel tread-rail top contact (for freight trains).
- High friction at the wheel tread-rail top contact (for locomotives), for greater traction.

Another area of surface transportation where friction plays an important role is that of automotive tyre-road interactions. Here, it is observed that the friction coefficient μ not only depends on the slippage s (this is identical to creep in Railway

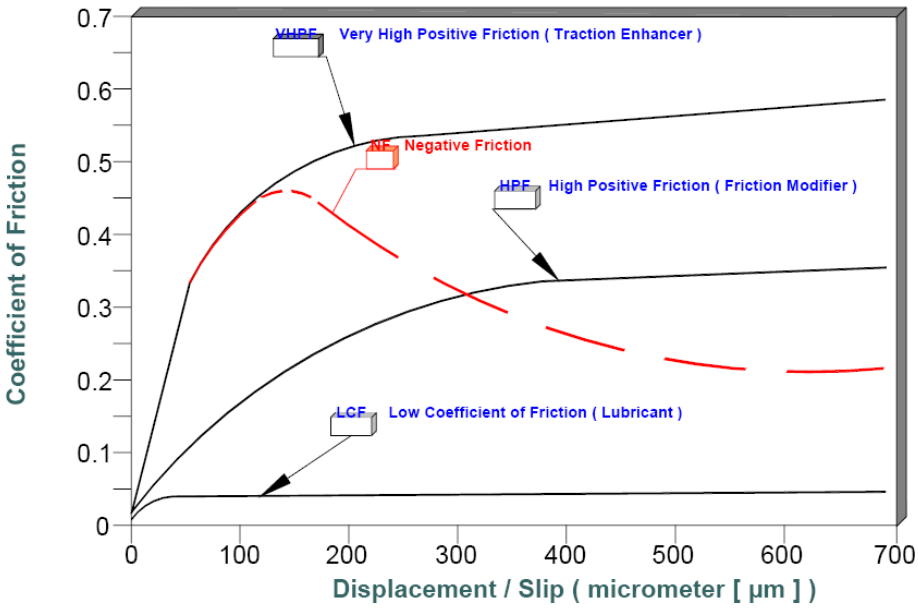

Figure 2.5: Frictional characteristics of different friction management products, LCF, HPF and VHPF [2].

literature) but also on the velocity v. A typical experimentally measured variation of μ with s and v is shown in Figure 2.6.

Returning to the railway systems, friction management through the introduction of a third body is achieved using the technologies already introduced earlier in Chapter 1. A particular modifier system of interest to the present study is based on solid stick technology. Just as the wheel-rail interface is prone to friction-induced instabilities so is the case with stick-wheel interface. To understand these instabilities a review of friction-induced vibration phenomena and their modelling will be taken up next.

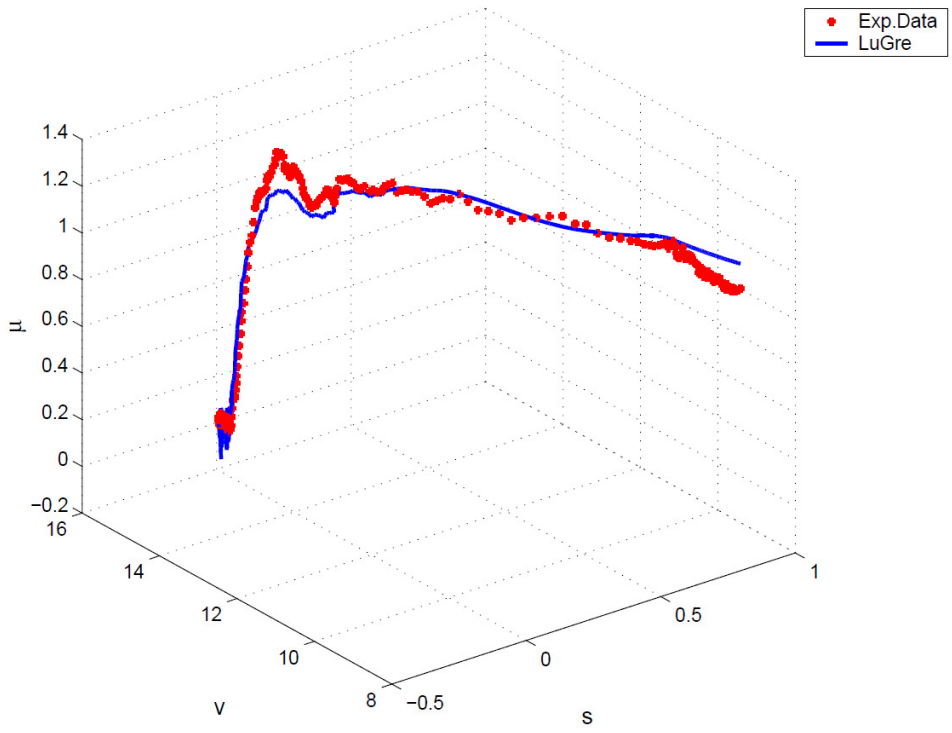

Figure 2.6: Three-dimensional plots of the (μ,s,v) curves measured on a car tyre, see [14] for more details.

2.3 Friction-Induced Vibration Phenomena

A vast amount of literature is associated with friction and associated vibrations. This is understandable as friction models are phenomenological in nature and several parameters such as temperature, contact pressure *etc.*, govern the friction between two surfaces in contact. Comprehensive reviews on friction-induced vibration in various engineering applications is provided by Ibrahim in [15] and [16]. A materials perspective on friction is given in the textbook by Rabinowicz in [17]. In addition, Feeny *et al* [18] gave an extensive historical review on dry friction and stick-slip phenomena, while a recent review by Akay [19] touched upon various aspects of friction and associated acoustics such as friction induced vibrations, friction sounds and waves in solids. Friction is examined from a control system design perspective in [7].

Self-excited friction-induced stick-slip vibrations have been widely discussed in the literature due to their presence in many sliding mechanical systems. Stick-slip phenomenon arises due to alternating elastic and plastic deformation mechanisms in the contact zone. First, an elastic deformation takes place where the two surfaces in contact are sticking (asperities deform elastically), then follows a plastic deformation where sliding takes place (asperities deform plastically). The most commonly accepted cause for the occurrence of stick-slip is the fact that there is a difference between static and kinetic coefficients of friction. It has been observed that friction coefficient decreasing with increasing sliding velocity is also responsible for stick-slip motion.

Stick-slip oscillations have been studied using the time dependence of static friction [20] and the kinetic friction-velocity characteristics of the sliding surfaces. Rabinowicz [21] states that sliding systems with negative friction-velocity characteristics give rise to the stick-slip oscillations between surfaces already in relative motion is equivalent to the negative friction characteristic that arises in systems starting from rest due to the static friction coefficient exceeding the kinetic friction coefficient.

Rabinowicz [21] gave a displacement criterion for the initiation of stick-slip process. This *'critical distance'* concept states that there exists a lower limit to the distance slid during the slip stage of the order of 10^{-3} cm and that stick-slip cannot occur if the distance that would be slid is less than this figure. Brockley, Cameron and Potter [22] studied the mechanisms of friction induced vibrations analytically and experimentally . They came across the existence of a *'critical velocity'* above which the stick-slip vibrations die out. This critical velocity was found to be dependent on damping, load, stiffness and time and velocity dependent friction characteristics.

Nakai and Yokoi extensively studied the mechanisms of frictional noise in Railway systems in a series of papers [23–27] with experiments on a pin (in the form of a cantilever beam) in contact with a rotating disc. They found that vibrations and associated squeals occur not only in areas with negative friction-velocity slopes, but also in areas with positive friction-velocity slopes. To explain this observation, they introduced the concept of instantaneous coefficient of friction to account for the squeal noises that may arise even when the slope of friction-relative velocity

curve shows positive characteristics. The instantaneous coefficient of friction is defined as the ratio of instantaneous friction force to instantaneous normal force. Over one cycle, this instantaneous coefficient of friction forms a loop whose orientation need not follow the steady friction-velocity characteristic obtained from the ratio of averaged friction and normal forces. Thus, even if the system has positive friction characteristic in the *average* sense it can be unstable due to the instantaneous friction-velocity characteristic being negative.

Chen and Zhou [28] studied the correspondence between the negative friction-velocity slope and squeal generation under reciprocating sliding conditions. Friction was found to be strongly dependent on both displacement and frequency of reciprocating sliding. Vibrations and associated squeals were also observed with positive friction-velocity slopes but no explanations were provided.

There are strong inter-connections between friction-induced vibrations in solid stick systems and disk brake squeal. Both these class of problems have two subsystems coupled via a contact with friction.

2.3.1 Disk Brake Squeal

Seminal research was conducted by Jarvis and Mills [29]. They presented experiments on friction-induced vibrations of disk brakes idealized as pin-on-disk systems. The apparatus used is shown in Figure 2.7 which comprises a rotating disc in contact with a metal bar. The contact is unlubricated and the consequent dry friction coefficient can strongly depend on the relative velocity. This velocity dependence leads to a set of coupled non-linear second order differential equations in the modal amplitudes of the two subsystems when a single mode of the disc is coupled to a single mode of the bar via a frictional contact. These coupled equations were derived by them and then solved in time domain by treating the pin as a cantilever beam and the disk as a thin plate. It is found that stability is intimately related to the angle of the bar, relative damping ratio, coefficient of friction and the mode of vibration of the components. The main conclusion form this work is that the geometry of coupling and the constitutive friction law play an important role in governing the stability of coupled subsystems, each of which is stable on its own in the uncoupled limit. This work paved way for future researchers to further

investigate friction-induced instabilities [30] and more recent work can be found in [31–35].

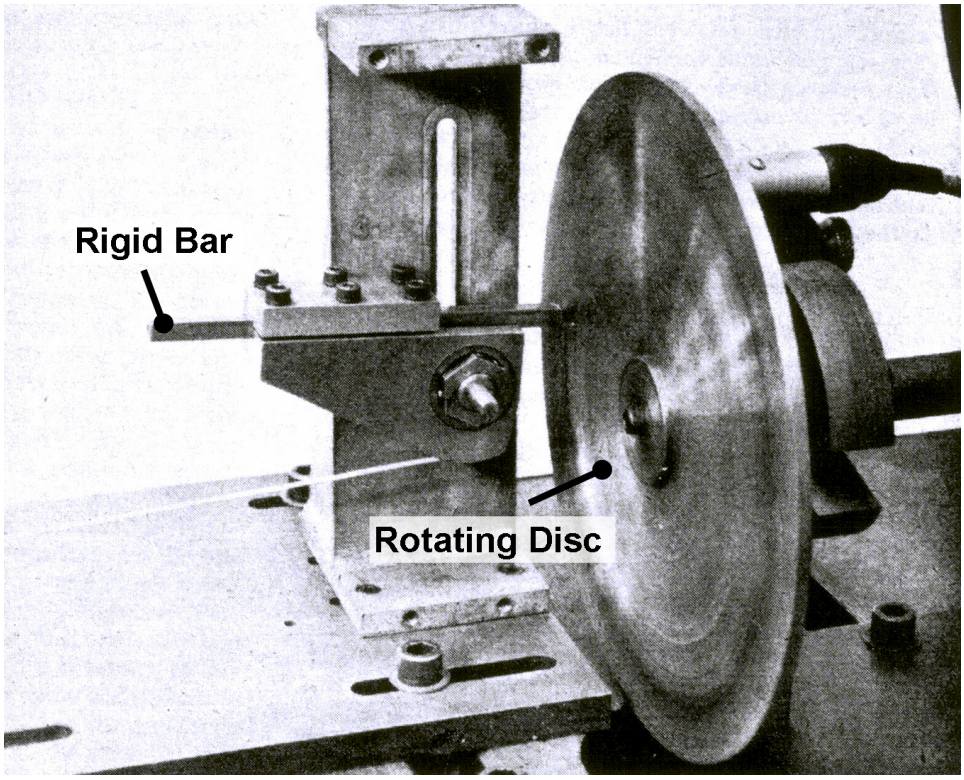

Figure 2.7: Pin-on-disk model of a disk brake studied by Jarvis and Mills [29].

Frequency response based stability prediction of coupled sub-systems is proposed by Woodhouse, Duffour and Butlin [6, 36–38]. These frequency domain methods can be readily used in industrial practise since sufficiently mature experimental modal analysis techniques exist to measure Frequency Response Functions (FRFs) [39]. Duffour [36–38] studied the stability of two systems, coupled by a sliding point contact by combining the modal analysis and a linear stability theory. He approached the classical Pin-on-Disc systems from a transfer functions perspective. Even with a simple contact model based on Coulomb's law of friction, a stability criterion was established. The model was also extended to account for the velocity dependent friction. Extensive experiments were also performed over a

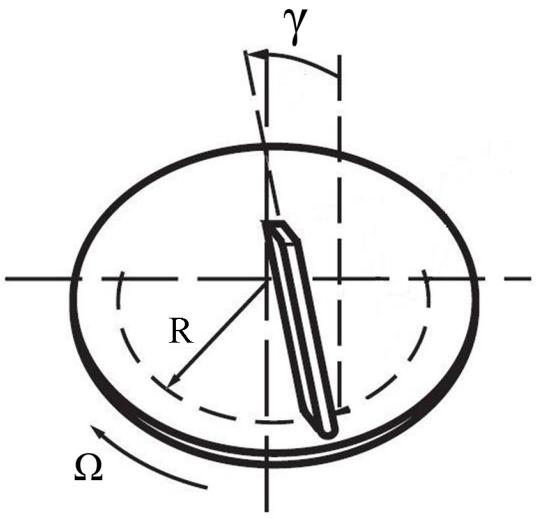

Figure 2.8: A model of the cantilever-disc system studied by Jarvis and Mills in [29].

course of time with reasonable, but not entirely conclusive results. Tore Butlin [6] extended the research to explain the sensitivity and uncertainty of predictions to parametric uncertainties. The FRF based stability prediction methodologies will be revisited in Chapter 3.

2.3.2 Railway Noise

Railway noises in general, can be classified into three categories. Firstly, the rolling noise, which is caused due to the uneven contact surface between the rail and the wheel. The existing roughness sets up the vertical vibrations. Then there is impact noise, which is an extreme form of rolling noise, produced when railway wheel runs over train joints and other form of discontinuities, particularly at crossings. This is also a vertical excitation, with non-linearities playing a predominant role. Lastly, the most troublesome is the squeal noise which occurs at sharp curves and involves lateral excitation mechanisms.

Hemsworth [40] conducted a thorough review on wheel-rail noise research (published till 1976). The review suggested that surface roughness is supposed

to be just one of the several parameters responsible for rail/wheel contact forces. Ten Wolde and Van Ruiten [41] continued the review of studies on sources and mechanisms of wheel/rail noise. Their review focussed on the importance of the effects of horizontal and vertical forces in the examination of wheel and rail excitation. Bender and Remington [42] studied the contribution and influence of sound generated by rails to the total noise levels.

Remington *et al* [43–45] performed a comprehensive work on the mechanisms of wheel-rail noise generation mechanisms, particularly, the rolling noise and curve squeal. Analytical models were developed for the prediction and on-field validation of squeal, impact and rolling noise. The analytical model was also improvised to accommodate the effect of changes in several rail/wheel system parameters.

The roughness conditions existing between the rail and the wheel cause both rail and wheel to vibrate and generate noise. The TWINS (Track-Wheel Interaction Noise Software) prediction model [46], designed by Thomson assumes that rail and wheel roughnesses are random and uncorrelated and hence their spectra can be added (in an energy sum). Dings and Dittrich [47] worked on the Dutch Railway Network to determine absolute roughness levels i.e., the contribution of rail and wheel roughness to the total roughness. They found a good correlation between the roughnesses and radiated rolling noise. Also, their experiments suggested that rail and wheel roughnesses contribute equally to the total noise. Rail corrugations which are supposed to occur locally were an exception to the rule.

Sato and Matsuhisa [48] studied the vibrations of train wheels and their relationship with the radiated noise. A rolling wheel experiment was designed to simulate the actual rail-wheel interaction. The experiment essentially consisted of two wheels pressed against each other at the circumference. Theoretical modelling was also undertaken by assuming the wheel as a hollow circular plate with fixed inner circumference and free outer circumference. A point on the outer circumference was simply supported to model the rail contact. Experiments showed a good agreement with the theoretical analysis and thus substantiated the model. It was also established that noise was caused by the axial vibrations of the wheel and vibration appears due to the rail-wheel interaction. In a subsequent work [49], they incorporated additional parameters: speed (rate of rotation) and load to investigate vibration frequency distribution and peak values in wheel vibrations and associated

noise. A coefficient of sound radiation (ratio of radiated acoustic power to mechanical power of the vibrating wheel) was also introduced to study the characteristics of sound radiation. They concluded that load does not have a significant effect on the vibration characteristics and sound levels. However, both increase with an increase in the rate of rotation. In the last paper of the series [50], they included the effects of shear deformation and rotatory inertia to account for the thickness of the wheel. Theoretical models were developed by assuming a circular plate with stepped thickness to model web and rim of the wheel. The results compared very well with the experiments performed on a Japanese rapid transit train (Shinkansen) wheel.

The most comprehensive review on rail wheel dynamics is credited to Thompson who surveyed a majority of aspects related to railway-wheel noise and vibration generation mechanisms in a series of papers [51–55]. Friction was found to play a major role in the railway noise and wheel-rail interactions. The solid stick flange lubrication system is primarily designed to mitigate lateral forces, wear and squeal at curves. It is therefore necessary to understand the physics of contact mechanisms prevalent at curves. The next section will describe the fundamentals behind the curve squeal.

2.3.3 Curve Squeal

While travelling through a curve, the outer wheels of the train need to travel a farther distance as compared to the inner wheels. Unlike automobiles, where a differential is used, the railway wheels are slightly tapered conically from outside. This allows the outer wheels of the train to ride on a larger diameter curve than the inner ones. On sharper curves, such conicity of railway wheels is insufficient to compensate for the added distance the outer wheel needs to travel. This causes a differential slip between the inner and the outer wheels. It is also important to note that there is no contact of the wheel flange with the gauge face of the rail when the curve radius is large. However, while moving over sharper curves, rail and wheel flange contact occurs causing ‘flanging noises’ which usually are of high frequency and occur intermittently.

Usually two or more wheel sets are present in a single rail-car or bogie, which

are constrained to move parallel and thus cannot align with the curve radius efficiently. Yaw angle (see Figure 2.9) which is described as the angle of attack of the front wheel set relative to the rails is high. This leads to high flange forces, noise and in worst cases, derailment can occur. Therefore in practise, wheel sets are optimized for flexibility so that they can align with the curve as much as possible.

The curving behaviour of the rail-cars is dependent on several parameters: speed of the train, radius of the curve, inclination of the track and the wheel-rail profile. Yaw angle is found to be larger for low speeds and for sharper curves. The wheel tries to roll straight ahead but is constrained to move along the curve. This causes the wheel to slide across the rail. Hence the squeal noise is believed to arise from such a lateral crabbing motion.

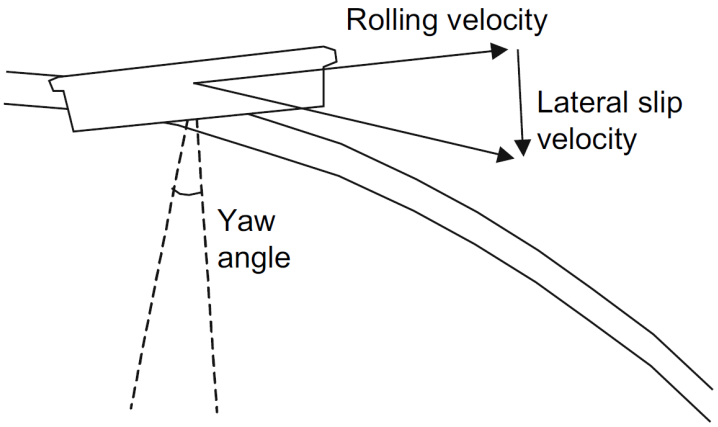

Figure 2.9: Generation of lateral creepage by a non-zero yaw angle [56]

Rudd [57] presented a model for the squeal of subway trains transversing tight curves. He considered three models for the mechanism of wheel squeal. They were:

1. Differential slip between inner and outer wheels on solid axle (when coning is insufficient, on tight curves).
2. Rubbing of wheel flange against the rail.
3. Crabbing of the wheel across the top of the rail.

He assumed that the crabbing motion to be the root cause of wheel squeal, wherein the exciting forces are normal to the plane of the wheel. The other two mechanisms were discredited in the analysis. The model was then used to predict squeal based on the speed of the train, curve radius and bogie/truck length. It was also found that wheel damping and rail lubrication effectively reduced wheel squeal.

Heckl studied the curve squeal of train wheels in time [58] and frequency [59] domains. She introduced a form of active control [60] for eliminating curve squeal. This method involves a feedback system to prevent the unstable wheel oscillations.

Popp, Schneider and Irretier [61] also studied the bending vibrations of railway wheels on sharp curves. They performed a finite element modeling of railway wheel. Modal expansion techniques were used to determine force and self-excited oscillations followed by calculations on sound levels and acoustic characteristics. Finally, the comparison between several kinds of wheels indicated strong dependency of sound on design parameters of the wheel. Their work assumed rigid rails and point contact between the wheel and the rail. Fingberg [62] extended their work by introducing track dynamics in the model and validated the numerical results through experimental measurements. Van Ruitten [63] measured the squeal noise radiated from several tram types across Dutch railway network. The analytical model proposed by Rudd [57] was then confirmed for parameters such as curve radius, rolling velocity, wheel load friction characteristics and damping.

It can be concluded that friction modification at curves has a significant influence on squeal, wear, and lateral forces. Thus far, the additional features in the response of a wheel arising due to rotation have not be explicitly considered. The next section surveys the literature on rotating disks.

2.4 Vibrations of Rotating Disks

The study on the classical problem of vibrations of a rotating disk goes back to 1829 when Poisson presented his memoir on vibrations of circular plates to French Academy of Sciences. In early 1850's, Kirchoff extended Poisson's results to his work on the vibrations of non-rotating disks. Airey [64] analysed the vibrations of circular plates considering fixed as well as free circumference and their rela-

tion to Bessel functions. Lamb and Southwell [65] investigated the vibrations of a completely free spinning circular disk taking into account the centrifugal stiffening due to rotation of the disk, neglecting the flexural rigidity. In his following work, Southwell [66] investigated the free transverse vibrations of a uniform circular disc clamped at its centre. He presented exact solutions for limiting cases, obtained by neglecting in turn, the centrifugal stiffening and the flexural stress-systems followed by an approximate analysis for a general case, when both centrifugal tensions and flexural stiffness are considered.

Bhuta and Jones [67] analyzed the vibrations of a thin, rotating circular disk using undeformed coordinates and found that rotation tends to lower the natural frequencies of the disk. Chen and Jhu [68] worked on the in-plane oscillations and stability of a spinning annular disk and emphasized the effect of clamping ratio on the natural frequencies and critical speeds of the spinning disk. Deshpande and Mote [69] studied the underlying physics behind the in-plane vibrations in thin rotating disks. They used a non-linear strain measure to calculate the strain energy of the deformed disk and thus captured the centrifugal stiffening of the disk due to rotation . The papers by Baddour and Zu [70, 71] reviewed spinning disk models. Hutton [72, 73] worked on the vibrational response characteristics of a circular saw blade, which can be viewed as an axisymmetric rotating disc and is widely used in wood cutting industry.

The most notable work on the vibrations of *stationary* and *rotating* circular disks was that of Tobias and Arnold [74]. The free vibration of a stationary perfect disk fixed at its centre is visualized as a stationary vibration, or a linear combination of a positive and negative travelling waves. The symmetry existing in a *stationary* circular disk leads to mode-pairs or double modes occurring at identical natural frequencies. The mode-shapes associated with the degenerate modes are similar or congruent. Whenever axial symmetry exists in a disk, the position of nodal diameters is arbitrary. The general expression for the vibration amplitude for such a disk vibrating freely and having n nodal diameters is:

$$u = a_1 f_n(r)\cos n(\theta-\beta)\cos(\omega_n t-\varepsilon_1) + a_2 f_n(r)\sin n(\theta-\beta)\cos(\omega_n t-\varepsilon_2) \quad (2.2)$$

This equation represents the superposition of two similar or congruent modes

of vibrations for natural frequency ω_n. $f_n(r)$ is the vibration displacement function along the radial direction. Angle β decides the arbitrary position of nodal diameters. The two nodal configurations are separated by an angle of $\pi/2n$.

On the other hand, in the presence of imperfections in the disk, degenerate modes of identical natural frequency split into two single modes each having distinct natural frequencies and different unique mode-shapes. For each forcing frequency, we have two different configurations i.e., superposition of two preferential modes.

In order to understand the behaviour of *rotating disks*, it is convenient to define a co-ordinate system, one which is fixed to the disk and the other fixed in space. A coordinate transformation can then be carried out to switch between the reference frames. When we consider free vibration of rotating disks, due to centrifugal stiffening, the natural frequencies of rotating structures increase with the speed of rotation. It is found experimentally that the following relation holds true:

$$\omega^2 = \omega_o^2 + B\Omega^2 \tag{2.3}$$

where ω is the frequency at rotational speed Ω , ω_o is the frequency of the stationary disk and B is some constant. However, in case of forced vibrations, the forcing frequency is replaced by two frequencies, $(\omega + n\Omega)$ and $(\omega - n\Omega)$ as opposed to stationary disks. Therefore, we have two pairs of resonant conditions for each mode of vibration. A typical frequency-speed diagram is shown in Figure 2.10 . Mode splitting will be seen later in Chapter 5.

2.5 Conclusions

This chapter has surveyed literature pertaining to friction and friction-induced vibrations. Modelling friction is a challenging task because of its dependence on several factors such as material properties, sliding speed, roughness, temperature, normal load and contact surface type which tend to make the system non-linear.

Friction induced vibrations on solid stick systems is a very complex, and to date, unpredictable phenomenon. Significant capital investment is required to outfit a fleet of trains with solid stick technology and if excessive vibrations are found, significant resources are required to ameliorate the problem. A stability prediction

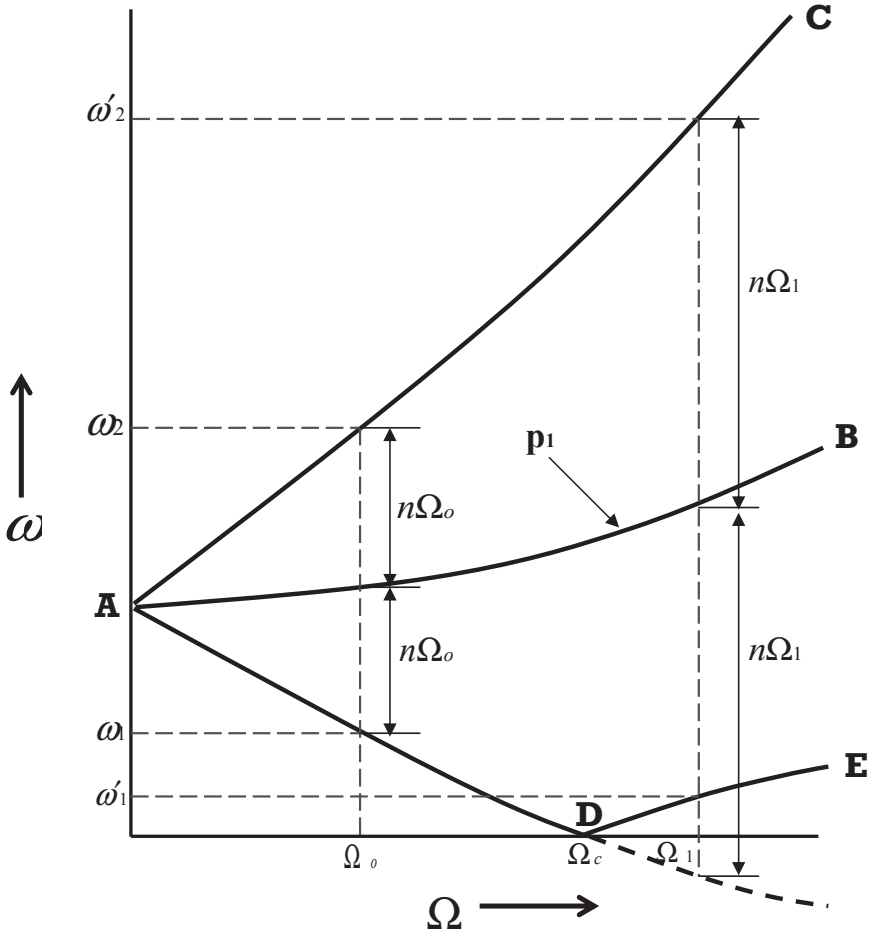

Figure 2.10: A typical frequency speed diagram : AB represents the variation of natural frequency p_1 with Ω, while AC and AD represents the resonant conditions $\omega = p_1 + n\Omega$ and $\omega = p_1 - n\Omega$, *Tobias 1957* [74]

methodology in the design stage is highly desired.

Stick vibration problem is a friction-coupled phenomenon with close parallels in disk brake squeal and railway noise literature. Frequency domain methodologies are deemed to be a suitable starting point which sets the scope of this work.

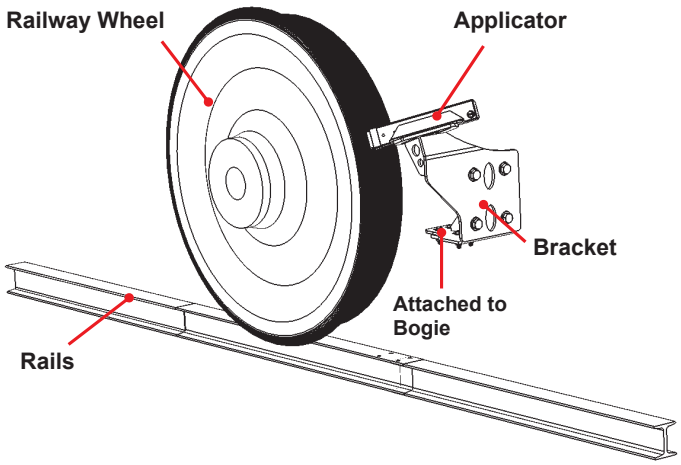

Figure 2.11: Wheel-applicator-bracket system.

2.6 Scope and Outline

The objective of this research is to develop a stability analysis procedure for the wheel-applicator-bracket system as shown in Figure 2.11 and compare the stability characteristics of different applicator-bracket designs in a virtual environment. Three candidate bracket designs are compared for the same applicator and friction modifier material. A first order model is developed using frequency domain analysis techniques with the aim of generating stability maps in the parameter space defined by the identified design parameters in Chapter 3. A detailed finite element modelling of the applicator-bracket-wheel system is undertaken in Chapter 4 to determine the parameters required for stability calculations. Vibration experiments are performed on available full-scale wheel test-rig to substantiate the FE models. FE Models can also incorporate design modifications to the bracket and applicator and thus they are essential for virtual designing. The final results are presented and explained in the form of stability diagrams in Chapter 5 indicating the operating conditions such as speed of train, angle of applicator, and coefficient of friction. Salient features of each chapter are pictorially summarized in Figure 2.12 which depicts the essential developments of each chapter leading up to stability maps.

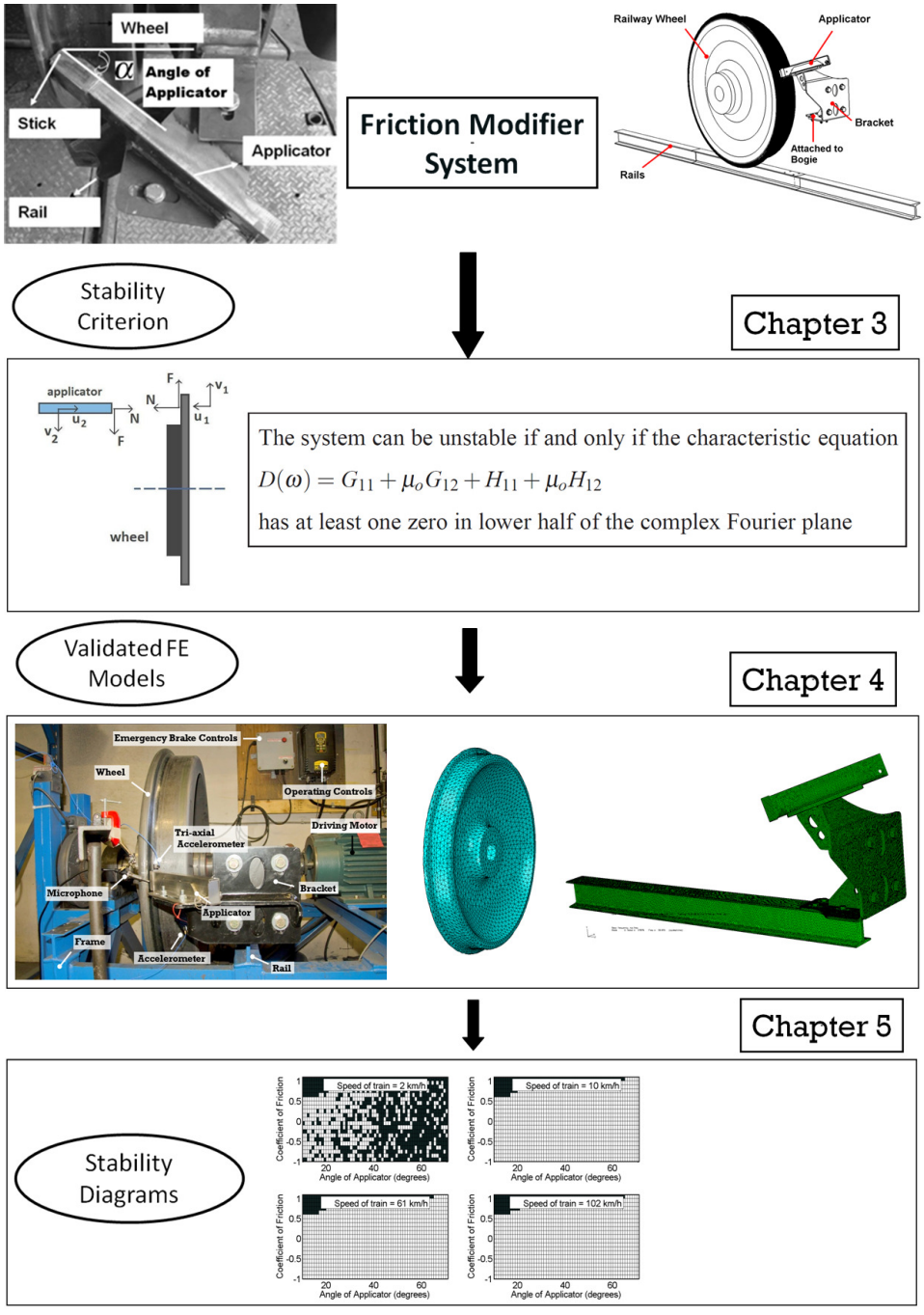

Figure 2.12: A pictorial overview of this dissertation.

Chapter 3

Stability Analysis

3.1 Introduction

Friction-induced vibrations are unstable in the sense that small amplitude oscillations build up over a period of time leading to excessive vibrations and noise. Chatter of solid stick friction modifiers is one such instability. This chapter develops a stability algorithm in frequency domain based on the closed-loop-transfer function (CLTF) of the two individual subsystems(wheel and applicator-bracket assembly) coupled via a sliding friction contact. Design considerations of friction modifier systems and the essential parameter of interest governing stability are identified in Section 3.2. There, the necessity for modelling simplifications will be seen given the availability of data and complex contact conditions prevalent *in situ*. A first order simplified model of wheel-applicator-bracket assembly is presented in Section 3.3. Linear stability analysis is then conducted for determining the stability in frequency domain in Section 3.3.1. A stability criterion is developed based on the Frequency Response Functions (FRFs) of each subsystem and a simplified contact law. Finally, this chapter ends with a summary of procedure to predict stability, outlined in Section 3.4. Subsequent chapters will build on the procedure established in this chapter.

3.2 Design Parameters

The design process of the friction modifier systems is severely constrained. A typical system is shown in Figure 3.1.

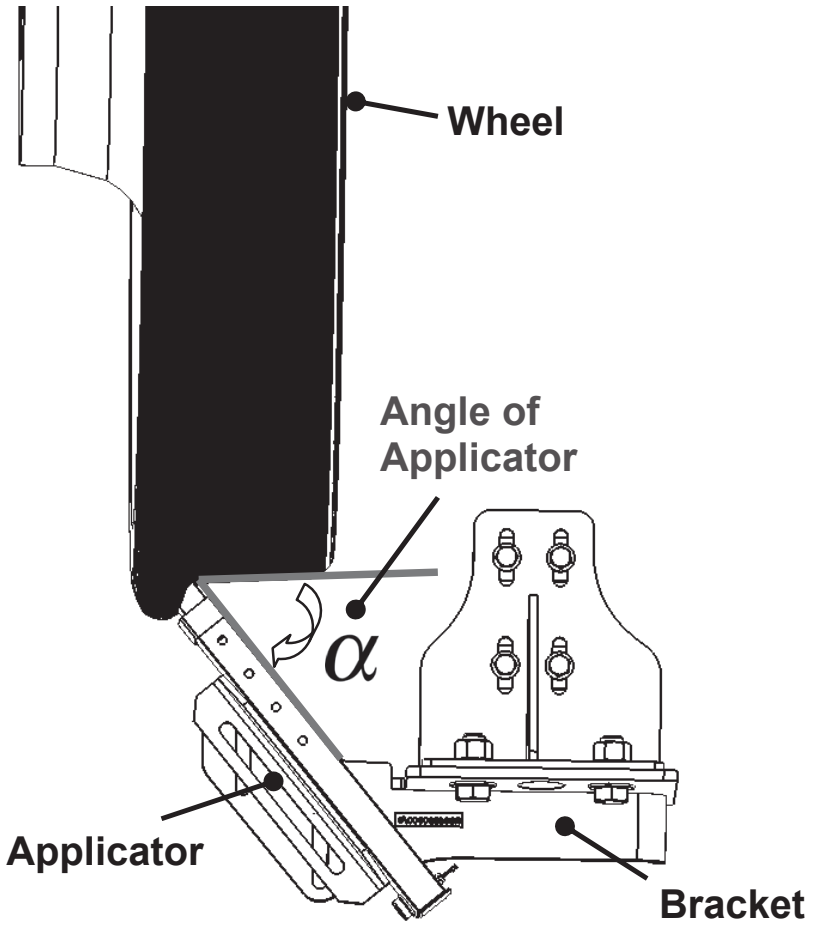

Figure 3.1: Plan view of the friction control system depicting angle of applicator, α for a particular applicator/bracket mounting configuration, which is parallel to plane of the ground

Space constraints on the trains for implementing such systems give designers little freedom to innovate. Presently, the designers use their previous experience to serve as a guide in designing newer brackets. This may not be optimal. Therefore,

a rapid and efficient tool that can compare the stability characteristics of different designs in a virtual environment is deemed necessary to avoid delays in retrofitting an unstable bracket-applicator assembly in the field.

In railway networks, the rail and the wheels have standard designs with minor variations. The applicator designs are also standard and limited in number, but brackets on the other hand are custom designed depending on the space available on the railway bogie where they are implemented. Different bracket designs are used across different railway networks. *It has been observed in field that for the same applicator design and similar mounting configurations, some bracket designs are more prone to self-excited vibrations than others. Therefore, the bracket design is important to consider.*

The parameters that determine the stability of friction control systems can be classified as follows:

1. **Geometric Parameters:** The solid stick friction control systems are applied onto the wheel flange at a particular angle depending upon the space constraints on the railway bogie. This angle of application of sticks can typically range from 20 to 70 degrees on a horizontal/ground plane with some angle in out of plane direction as well. Figure 3.1 shows an angle of applicator for a particular Applicator/Bracket mounting configuration, which is placed parallel to the plane of the ground. The angle of the applicator, α is measured with respect to the normal on the wheel flange at the point of contact. Angle of the applicator has been known to be an important factor that might contribute to the variation instability from the previous field experience.

2. **Contact Parameters:** The dynamic response of the moving wheel is coupled to that of the bracket-applicator assembly via sticks as shown in Figure 3.2. Coefficient of friction at the stick-wheel interface plays an important role in the stability characteristics of the system. It depends on both track and wheel roughnesses. Rail roughness is a random phenomenon as surface conditions change across different sections of the track, while wheel roughness is approximately periodic with respect to the circumference of the wheel. Besides, environmental conditions such as moisture, humidity, pressure, presence of contaminants like dirt and external particles influence the

surface conditions.

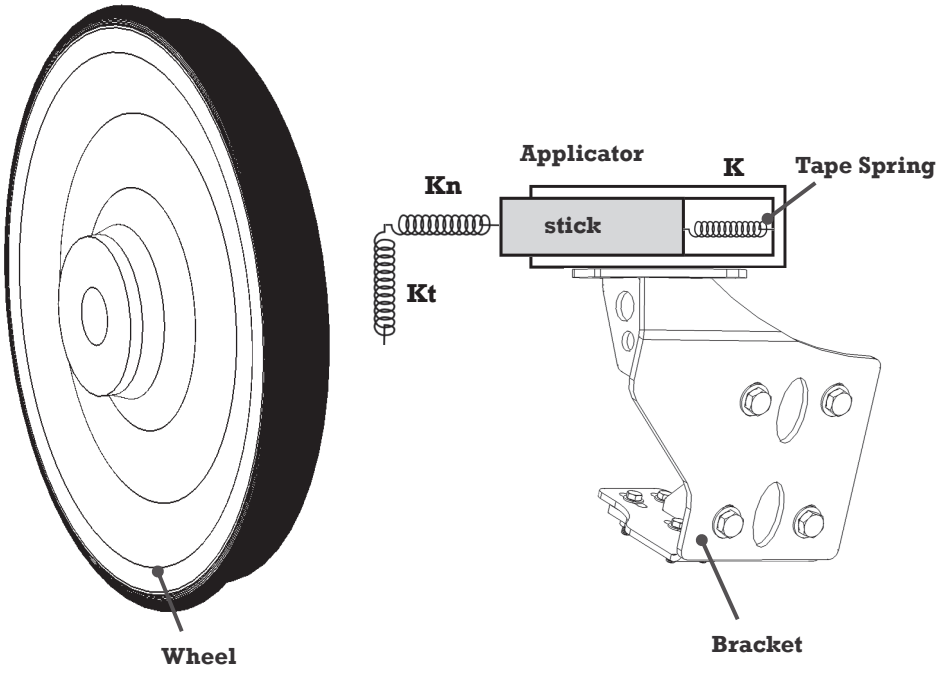

Figure 3.2: Applicator-wheel contact model

The material properties of the stick in use determine the contact parameters such as contact damping and stiffness at the stick-wheel interface. Besides, when the stick is applied on to the flange of the railway wheel, a constant force tape spring placed at the back of the stick always pushes it against the wheel (see Figure 3.2). This effectively influences the contact conditions at the stick-wheel interface and thus stiffness of the tape spring need to be taken into consideration as well. Modelling contact requires detailed knowledge about the tribological characteristics of the stick material, which is currently unavailable. Hence, the contact processes are simplified. *However, the same stability methodology which will be developed in this dissertation can be applied if refined contact models and data are available in the future.*

3. **Structural Parameters:** Consider the mounting configuration and attachment of the applicator/bracket assembly to the railway bogie in Figure 3.2. They influence the overall stiffness of the system. Structural properties of an applicator depends on its geometric dimensions such as length, thickness, and shape of cross-section. Moreover the dynamic response of the applicator might depend on the bending stiffness, damping, number of sticks present inside and the tape spring.

4. **Operating Parameters:** The speed of the train is yet another important parameter. The stability of the friction control system is largely influenced by changes in the train speed. From field observations, it has been noticed that lower train speeds make the system more prone to vibrations. Besides, the track can either be curved or straight depending upon the railway network.

In the model for the applicator-bracket subsystem shown in Figure 3.2, contact stiffness and contact damping parameters are still unknown and can be determined only through tribological tests. It has also been confirmed in practice that keeping same applicator and mounting configuration and just changing the bracket design highly influences the stability of system as whole. A robust contact model would be a part of future work. Currently, for simplified model, we plan to focus on a generic single point contact model of the coupled system ignoring the aforementioned contact parameters and sticks. This approach allow one to compare different bracket designs *qualitatively* for the same track, tape spring, applicator, stick configurations. The next section describes the frequency domain modelling of the coupled system.

3.3 Modelling in Frequency Domain

A simplified model of Applicator-Bracket-Wheel system is developed in this section using frequency domain stability analysis. The current modelling approach is motivated by the works of Duffour and Woodhouse [36] in the context of disc brake squeal problems assuming single point contact between components. The focus is to predict the onset of instability using linear stability theory. Figure 3.3 shows a simplified schematic diagram of applicator-wheel system coupled by a sliding

friction contact. The applicator here, represents the entire applicator-bracket assembly. The applicator is shown normal to the wheel for clarity and the angle of applicator is not normal in practice. This can be incorporated using a straightforward transformation matrix to transform equations from local normal-tangential co-ordinate plane of the contact to the global co-ordinates. In the interest of simplicity, the equations are developed for applicator normal to the wheel so that the local and global co-ordinates coincide. Certain assumptions are made to simplify the system, which are discussed next.

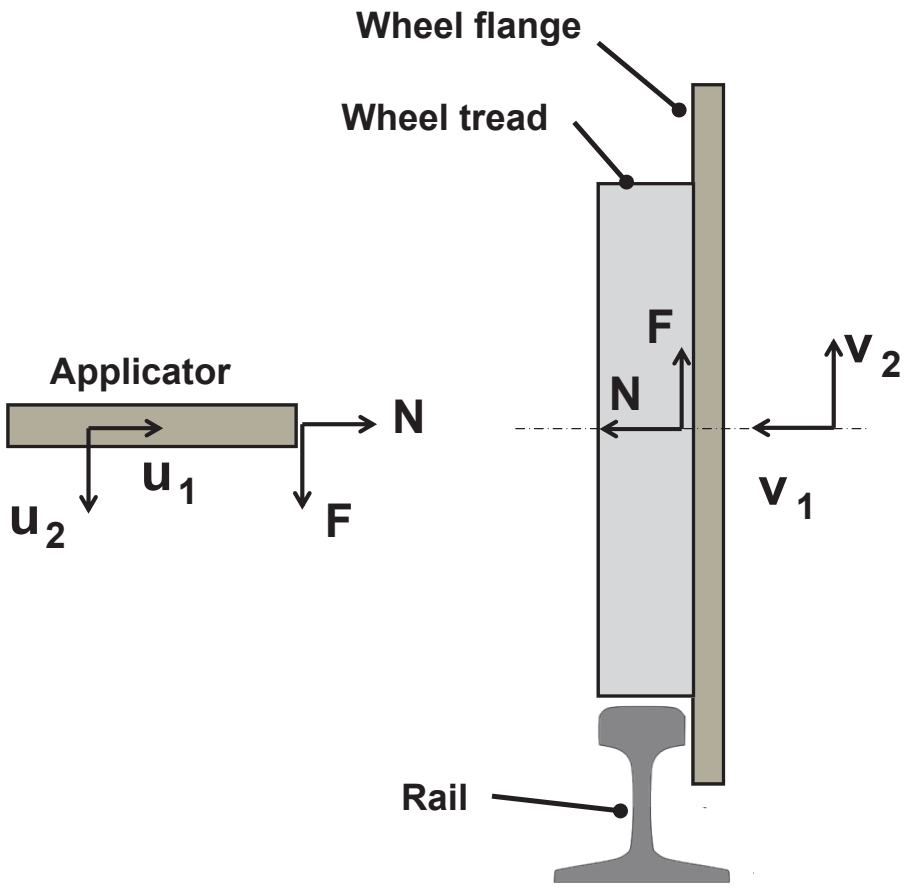

Figure 3.3: Schematic diagram of applicator-wheel coupled system indicating interacting forces and displacements at the contact point.

It is assumed that the onset of instabilities arise from steady stable operating state. Thus we ignore any unstable conditions which may arise due to the transients. This linearised stability analysis assumes that there is a single point contact between the applicator-bracket assembly and the wheel. No stick or tape spring is included in the model. The reason being, modelling the contact stiffness and damping would require detailed tribological data, which is not currently available. But the assumption can be relaxed at a later date when the required data is made available. *The stability analysis procedure however will remain the same*. With these assumptions, a frequency domain stability criterion will be established next.

3.3.1 Frequency Domain Stability Analysis

Consider Figure 3.3 in which the applicator and wheel subsystems exert a normal force N on each other. F is the corresponding frictional force. N_o and N' are the steady and fluctuating components of normal force, while F_o and F' are the corresponding friction force equivalents. The corresponding displacements at contact point are shown slightly away from the actual location for the sake of clarity. The following relation hold in Figure 3.3

$$N = N_o + N', \qquad |N'| \ll |N_o|, \tag{3.1}$$

$$F = F_o + F', \qquad |F'| \ll |F_o| \tag{3.2}$$

Displacements are related to forces in frequency domain via matrices of transfer functions. The matrix$\boldsymbol{G}$ represent the wheel transfer functions while the matrix $\boldsymbol{H}$ represent the applicator transfer functions. Using the first index in the subscript to indicate the degree of freedom corresponding to the input force, and the second index indicating the degree of freedom corresponding to the response of the subsystem, the frequency domain relations between the displacements and corresponding forces are:

$$\begin{bmatrix} v_1 \\ v_2 \end{bmatrix} = \begin{bmatrix} G_{11}(\omega) & G_{12}(\omega) \\ G_{21}(\omega) & G_{22}(\omega) \end{bmatrix} \begin{bmatrix} N' \\ F' \end{bmatrix} \tag{3.3}$$

$$\begin{bmatrix} u_1 \\ u_2 \end{bmatrix} = \begin{bmatrix} H_{11}(\omega) & H_{12}(\omega) \\ H_{21}(\omega) & H_{22}(\omega) \end{bmatrix} \begin{bmatrix} N' \\ F' \end{bmatrix} \tag{3.4}$$

Roughness present on the surface of the railway wheel is the source of excitation to the linear system. This surface roughness is denoted by r in this formulation. Assuming that the two sub-systems remain in contact, the two normal displacements are equal and opposite except for the roughness effect

$$v_1 = r - u_1 \tag{3.5}$$

The relationship between normal and friction force can be described by a coefficient of friction, which we assume to be of the form

$$F = \mu_o N \tag{3.6}$$

Introducing Equation 3.5 in Equation 3.4 along with the constitutive friction law taken as in Equation 3.6, the closed loop transfer function (CLTF) from input roughness to fluctuating component of normal force is obtained as

$$N = \frac{r}{G_{11} + \mu_o G_{12} + H_{11} + \mu_o H_{12}} \tag{3.7}$$

Denominator of the CLTF is the characteristic equation whose roots determine whether the CLTF of the two subsystems in contact is stable or not. Using concepts from control theory [75], the stability of the stick-wheel system depends on the roots or zeros of the characteristic equation. For a linear system to be stable, the zeros of the characteristic equation should lie in the upper half of the Fourier domain or in the left half plane of the Laplace domain. Thus stability criterion can be stated as :

The system can be unstable if and only if the characteristic equation $D(\omega) = G_{11} + \mu_o G_{12} + H_{11} + \mu_o H_{12}$ has at least one zero in lower half of the complex Fourier plane

(3.8)

Stability criterion can be expressed as a simple feedback loop, shown in Figure 3.4. Input to this block diagram is surface roughness r and output is fluctuating component of normal force N. The forward transfer function is the reciprocal of

the summation of G_{11} and H_{11}, while the feedback is coefficient of friction μ_o multiplied by the summation of G_{12} and H_{12}.

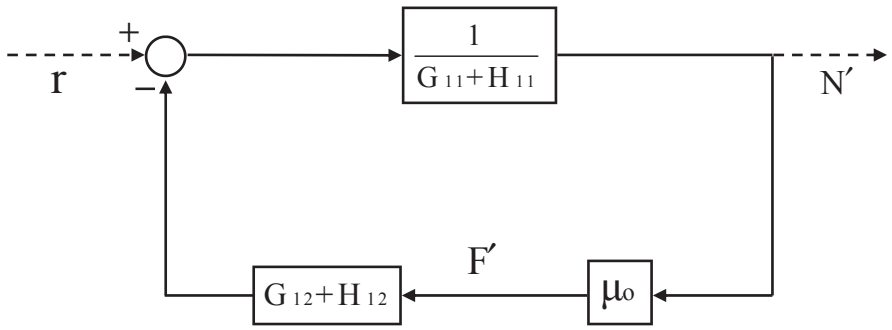

Figure 3.4: Block diagram of stability criterion

It is important to note that that any design changes in the bracket-applicator assembly will change the individual FRFs and in turn the stability of closed loop transfer function. Finite element/experiments will provide the individual FRFs. For example, changing the mounting bracket alters $\boldsymbol{H}$ transfer functions in the stability analysis. Since stability is being assessed in terms of poles and zeros it is worth recalling the control theory background.

3.3.2 Control Theory Background

In control theory, a transfer function (TF) is a representation of differential equation of the system and captures the dynamics of the system in frequency domain. In Laplace domain, it is essentially a rational function in s, where $s = \sigma + j\omega$ is a complex quantity, represented as a vector in Laplace or s-plane.

$$H(s) = K\frac{s^n + b_{n-1}s^{n-1} + b_{n-2}s^{n-2} + ... + b_o}{s^m + a_{m-1}s^{m-1} + a_{m-2}s^{m-2} + ... + a_o}, \qquad m > n \qquad (3.9)$$

Numerator and denominator polynomials can be factorised with the denominator being termed as the characteristic equation of the TF.

$$H(s) = \frac{N(s)}{D(s)} = K\frac{(s-z_1)(s-z_2)(s-z_3)...(s-z_n)}{(s-p_1)(s-p_2)(s-p_3)...(s-p_m)}. \qquad m > n \qquad (3.10)$$

The roots of the numerator are the zeros of the transfer function i.e., value of TF vanishes and they essentially represent the anti-resonances of the system. The roots of the denominator are the poles of the system i.e., value of TF becomes unbounded and they represent the resonances of the system. Thus poles and zeros govern the response of the system and hence its stability.

In general, the stability can either be Bounded Input Bounded Output (BIBO) or Asymptotic. BIBO stability occurs when a bounded input gives a bounded output, while in asymptotic stability, response emanating from initial conditions converges or dies out.

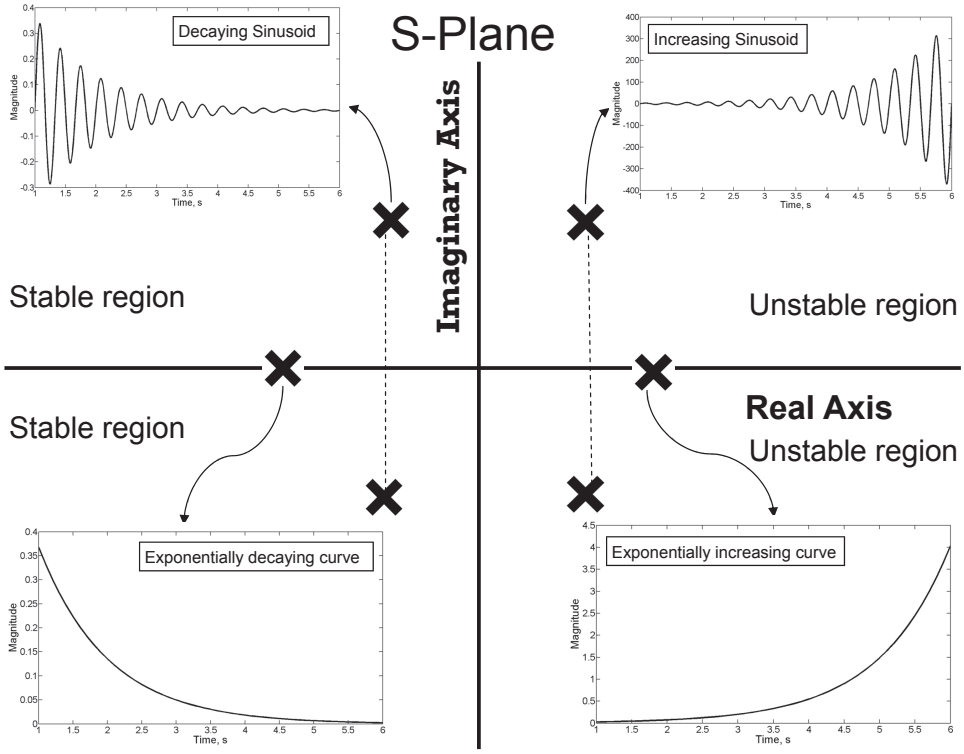

Figure 3.5: Stability regions in *s*-domain

Location of poles and zeros of CLTF give qualitative insight into the stability and transient characteristics of a system. Stability condition in *s*-domain states that all the poles of a stable TF are in the open left half of the complex plane (LHP). The term 'open' means that the imaginary axis is excluded. See Figure 3.5. Locations of poles of TF characterize the system response as follows:

1. When the pole is real and lies on the LHP of the Laplace plane (third quadrant in Figure 3.5), it indicates that the component has an exponential decay in response.

2. When the poles are complex conjugates of each other (pole-pair) and lie on the LHP of Laplace plane (second quadrant in Figure 3.5), it indicates that the component has a decaying sinusoid.

3. When the pole is real and lies on the RHP of the Laplace plane (fourth quadrant in Figure 3.5), it indicates that the component has an exponential increase in response.

4. When the poles are complex conjugates of each other (pole-pair) and lie on the RHP of Laplace plane (first quadrant in Figure 3.5), it indicates that the component has an increasing sinusoid.

5. When the pole-pair lie on the imaginary axis, it represents an oscillatory motion of constant amplitude depending on initial conditions. Imaginary axis poles essentially represent a marginally stable condition.

6. A pole at origin corresponds to the component having a constant amplitude depending on initial conditions.

In addition, the poles of the transfer function which are closer to the imaginary axis on LHP dominate the response behaviour as they correspond to slow decay components, while the poles away from the imaginary axis correspond to components whose response converges quickly.

In experiments Laplace transform is infeasible, and frequency response is measured. It is the transfer function evaluated on the imaginary axis of the *s*-plane,

$s = j\omega$. It gives the steady state response of the system after the transient dies out and is expressed as

$$H(j\omega) = K\frac{(j\omega - z_1)(j\omega - z_2)(j\omega - z_3)...(j\omega - z_n)}{(j\omega - p_1)(j\omega - p_2)(j\omega - p_3)...(j\omega - p_m)}, \qquad m > n \quad (3.11)$$

where $H(j\omega)$ is called the frequency response function (FRF). For each ω, FRF takes a complex number $H(j\omega)$, which has a gain and phase. FRFs can be graphically represented either by Bode Plots or Nyquist Diagrams [75].

In summary, the stability of a closed loop transfer function (CLTF) can be determined by the roots of the characteristic equation. Closed loop system is stable if the characteristic equation has all roots in the open LHP of Laplace domain, or upper half of the Fourier domain as illustrated in Figure 3.6.

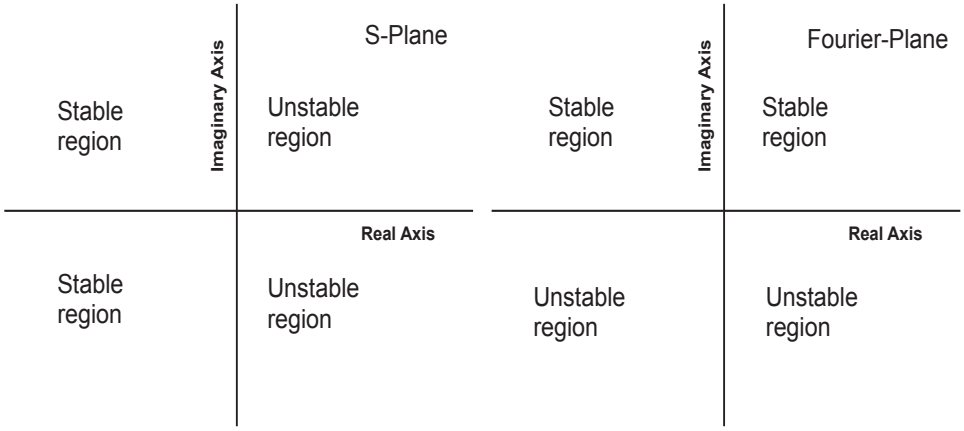

(a) Stability regions in Laplace Plane **(b)** Stability regions in Fourier Plane

Figure 3.6: Stability regions in Laplace and Fourier planes

3.4 Stability Prediction Methodology

Returning now to the characteristic equation $G_{11} + \mu_o G_{12} + H_{11} + \mu_o H_{12}$, the following observations can be made.

1. It contains the dynamics of the applicator-bracket assembly through $\boldsymbol{H}$ transfer functions and dynamics of the wheel through $\boldsymbol{G}$ transfer functions.

2. Any change in design of Applicator-Bracket assembly or any change in its orientation will influence $\boldsymbol{H}$ transfer functions, while any change in the speed of the train will influence $\boldsymbol{G}$ transfer functions.

3. The third parameter involved in the characteristic equation is the coefficient of friction μ_o, which has been assumed to be velocity independent i.e., it does not depend on the relative velocity of the sub-systems at the contact point.

Thus, transfer functions $\boldsymbol{G}$ and $\boldsymbol{H}$ along with the coefficient of friction, μ_o are the governing parameters for determining the stability of this system. Consequently any changes in these three parameters will influence the stability. Based on the above discussions, the following methodology, summarized schematically in Figure 3.7, can be adopted.

1. Compare transfer function matrices ($\boldsymbol{G}$ and $\boldsymbol{H}$) for wheel and applicator using modal analysis or finite element package like ABAQUS. These can also be measured if a prototype is available.

2. Curve fit FRFs to obtain numerator and denominator polynomials of Transfer Functions. Alternatively, use the modal parameters computed using FE to generate RFP form of FRFs.

3. Stability criterion Equation 3.8 gives a characteristic polynomial in ω.

4. Solve for the complex roots / zeros of characteristic polynomial.

5. System is unstable if any solution has a negative imaginary part.

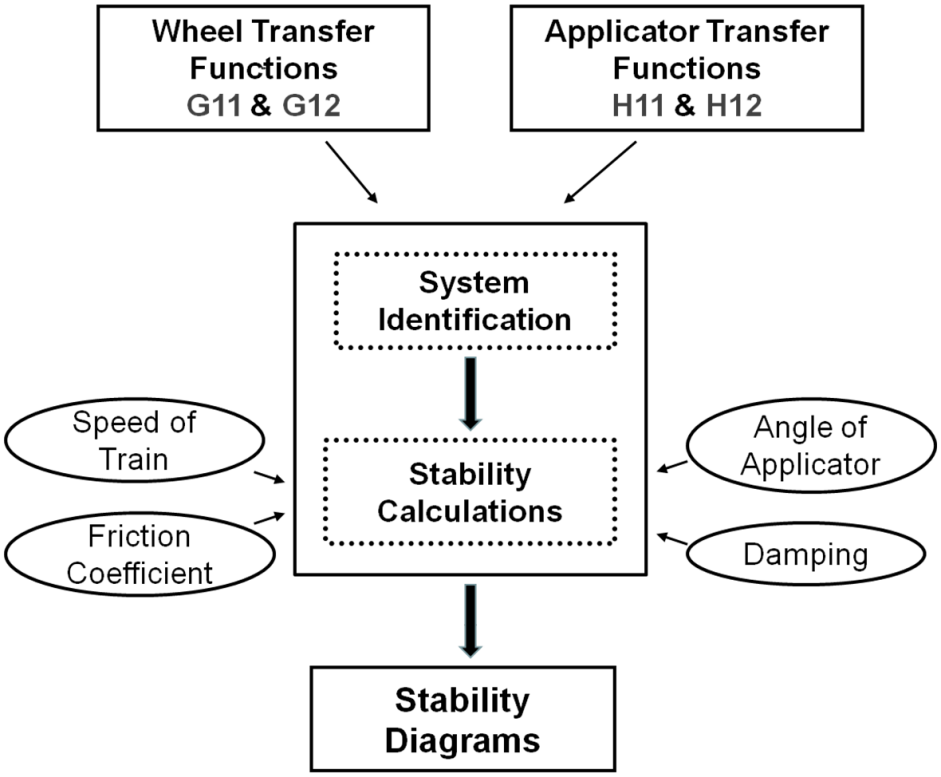

Figure 3.7: Flowchart for stability prediction methodology

3.5 Conclusion

A stability criterion is established based on the transfer functions of individual subsystems and a contact friction model, assuming constant coefficient of friction. The dynamics of both subsystems: wheel and applicator-bracket assembly are contained within frequency response function (FRF) matrices. Any changes in the speed of the train will influence the wheel transfer functions. This allows train speed to be one of the parameters for determining stability regions. Any change in design of the Applicator-Bracket assembly or change in the orientation of application will influence the applicator-bracket transfer functions. In addition, changes in contact model can arise due to changes in the value of friction coefficient. The stability is assessed by observing the location of closed-loop poles. Finally, the stabil-

ity diagrams can be obtained for the parameters of interest: coefficient of friction, angle of the applicator and speed of the train. The major advantage of using transfer function approach is the fact that it is model independent and is *measurable*. So any design change can be easily incorporated by the proposed methodology and comparisons can be made among several designs.

The next step would be to obtain the transfer function matrices for the individual sub-systems. Chapter 4 will focus on FE modelling and experiments. In Chapter 5 FRFs are computed using the modal parameters obtained from the experimentally validated FE models.

Chapter 4

Experiments and Modelling

4.1 Introduction

Frequency domain based stability analysis procedures have been established in Chapter 3. It is seen that the Frequency Response Functions (FRFs) of individual subsystems are required along with a contact law in order to assess the stability of the coupled system. FRFs can be measured either through experiments or predicted using Finite Element (FE) models. Usually FE models are preferred in a virtual design environment and in fact are the only availableFRFs prior to manufacturing. It is at this stage that the designer wishes to compare different bracket designs or changes made to an existing bracket configuration. In order to build confidence in the stability analysis, FE models need to be validated with experimental data. This chapter focusses on setting up experiments and developing the corresponding FE models with the aim to obtain valid models.

The chapter begins with an introduction to the Full Wheel Test Rig (FWTR) in Section 4.2.1 where the three candidate bracket designs are also introduced. This is followed by a description of experimental procedures and analysis of measured data on the FWTR for three different bracket designs in Section 4.2. Next, FE models of the wheel and three applicator-bracket assemblies are developed and discussed in the second half of the chapter in Section 4.3. Finally, the chapter concludes with comparison and validation of these finite element models with experimental results in Section 4.4, wherein the measured natural frequencies on the

FWTR are compared with FE predictions. The validated FE models obtained in this chapter will later be used later in Chapter 5 to compare the stability maps of three different bracket designs for the same applicator.

4.2 Experiments

It was seen in Section 3.2 that for the same applicator and stick designs the bracket has a pronounced effect on the stability based on the field observations. In this section three bracket designs are considered to test these observatons under controlled conditions on a Full Wheel Test Rig facility to be discussed later in Section 4.2.1. The three bracket designs, labelled as A, B, and C in Figure 4.1. These three bracket designs have been used with the same applicator. In order to use them in the FWTR facility, supporting brackets were made. All the brackets were mounted using bolted connections.

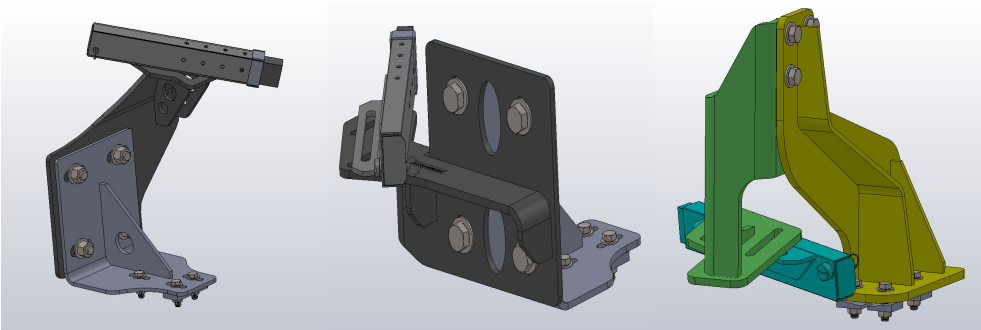

(a) Bracket Design-A **(b)** Bracket Design-B **(c)** Bracket Design-C

Figure 4.1: Bracket designs

4.2.1 Full Wheel Test Rig

The Figure 4.2 shows the Full Wheel Test Rig facility. The test rig essentially consists of two subsystems: wheel and the applicator-bracket-frame assembly mounted on a frame. The frame is designed to simulate the actual friction control system on the railway bogie. A railway wheel (0.9 m diameter) is mounted on an axle which is driven by a motor whose speed in turn can be controlled. An applicator

is mounted on the frame via the selected bracket design. The bracket is attached to an I-beam (labelled as rail in Figure 4.2) of the frame with the help of an additional support bracket. A triaxial accelerometer is placed at the top face of the applicator near the interface, while another accelerometer is placed on the bracket. A microphone is also placed near the stick wheel interface to capture the sound coming from the stick-wheel interaction. The top right corner in Figure 4.2 shows the controls for operating the motor. Safety features such as emergency brakes are also in place to avoid any mishap.

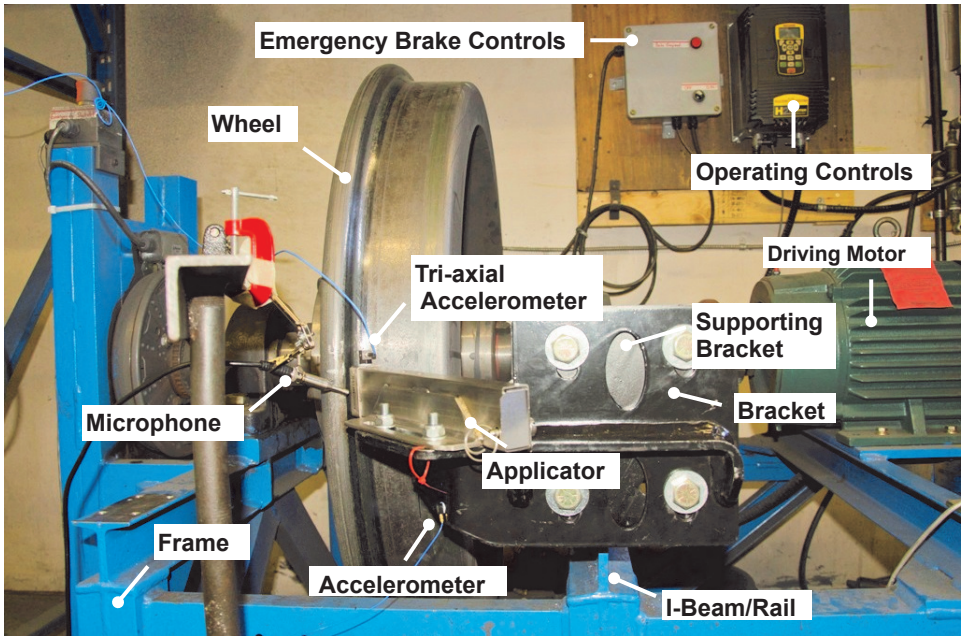

Figure 4.2: Full Wheel Test Rig

Experiments on the test rig are carried out in two stages: impulse tests followed by the operational tests, which involve the rotating wheel. Modal tests with an instrumented impulse hammer provides the information about the resonant frequencies, mode-shapes and damping characteristics of the system through a Frequency Response Function. A schematic of the signal flow is shown in Figure 4.3.

The system (Applicator-Bracket Assembly) to be tested is delivered an impulse by a modally tuned impulse hammer. The force signal from the hammer and the sensor signal from the accelerometers go into the signal conditioner, thence to

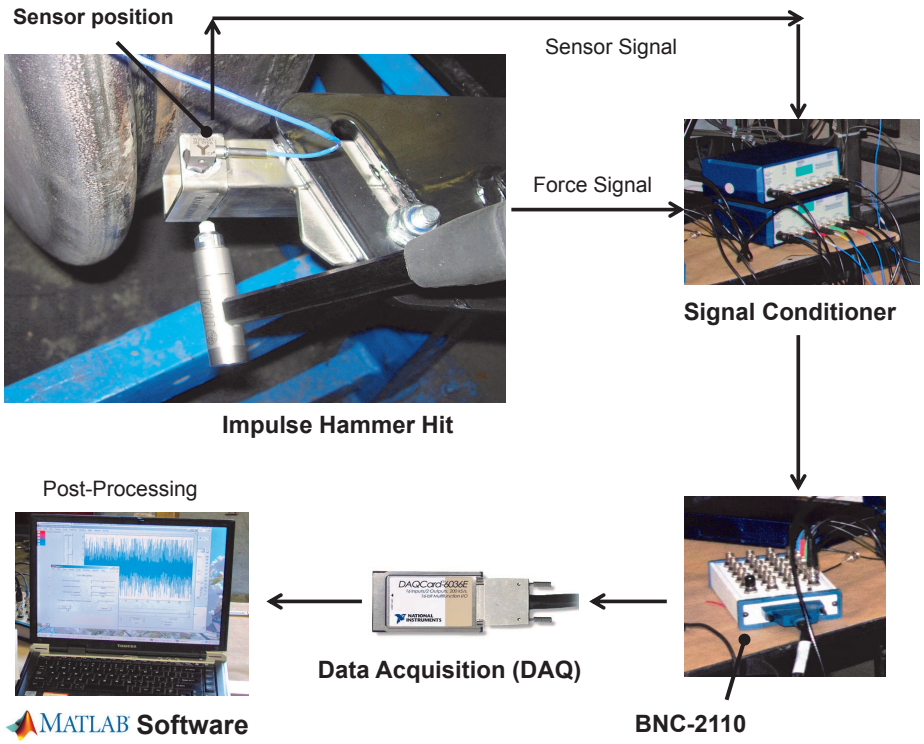

Figure 4.3: A schematic of the signal flow in experimental modal analysis

data acquisition system. An in-house data logging and post processing written in MATLAB©is used to analyse the acquired data.

4.2.2 Impulse Tests

For each of the applicator-bracket assembly tested, a triaxial accelerometer is placed on top of the applicator near the interface as shown in Figure 4.4. Y-direction of the accelerometer is the outward normal on the top surface; X-direction is along the length of the applicator and Z-direction is the outward normal in the lateral direction as shown in Figure 4.4. An impulse is given along each of these directions i.e. the top of the applicator near the interface; the side of the applicator near the interface in lateral direction and along the axis of the applicator. The response is measured by the tri-axial accelerometer.

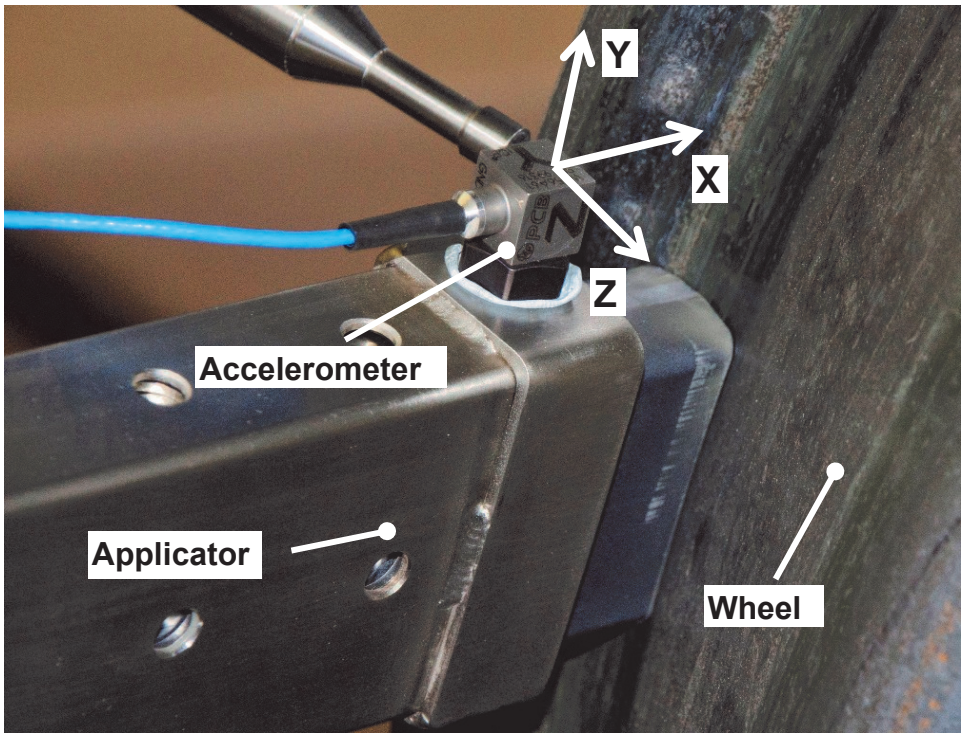

Figure 4.4: Co-ordinate directions represented by tri-axial accelerometer

The impulse tests were performed on all three available applicator-bracket assemblies: Bracket Design-A, Bracket Design-B and Bracket Design-C as shown in Figure 4.5. Bracket Design-A and Bracket Design-B are attached to the rail of the frame through the same supporting bracket, while a different supporting bracket is used to mount Bracket Design-C as shown in Figure 4.5. An additional accelerometer was kept on the corresponding brackets to capture the transmitted vibrations.

The test configurations for the three bracket designs and the wheel are shown in Figure 4.5

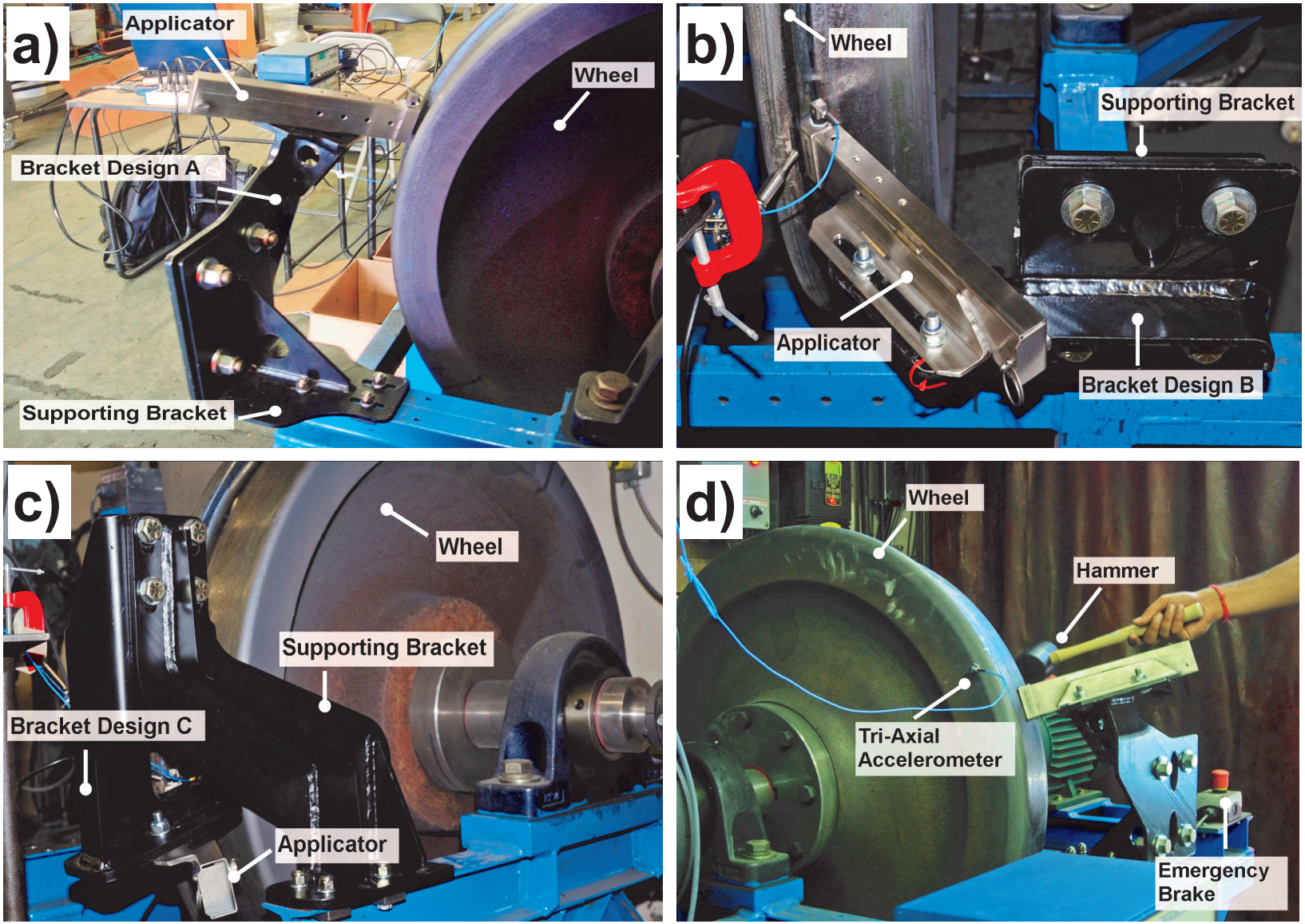

Figure 4.5: Experimental setup for (a) Bracket Design-A, (b) Bracket Design-B, (c) Bracket Design-C and (d) Wheel. Note that Bracket Design-C has a supporting bracket different from that of A and B which have the same supporting bracket.

An ideal impulse has an infinitesimally small duration of contact resulting in a constant amplitude in frequency domain. It excites all modes of vibration with equal energy. But in practice, an impact hammer strike has a small but finite duration of contact time. The contact time determines the bandwidth of the force in frequency domain. A smaller contact time ensures a larger bandwidth and vice-versa. So, it is always ensured that the contact time with the hammer is small and there are no multiple hits from the impulse hammer. As an impulse signal exists for a very short duration, pre-trigger delay ensures that the entire signal is captured. Modal Tuning is another important attribute of an impulse hammer that ensures the structural characteristics of the hammer do not affect the measurements. This is achieved by avoiding hammer resonances in the frequency range of interest, thus resulting in accurate and consistent measurements.

The data is first measured and displayed as a time signal, a typical impulse test data is shown in Figure 4.6. A good impulse can be seen by looking at the force signal in time domain and ensuring that no multiple spikes are detected. Fast Fourier Transform (FFT) then converts the time domain signal into frequency domain to give spectra for the impulse and the acceleration responses. The ratio of the output to input spectrum then gives the FRF for the system. A typical drive point FRF measured at the tip of the applicator is shown in Figure 4.7, wherein the peaks indicate the natural/resonant frequencies of the system and troughs indicate the anti-resonances.

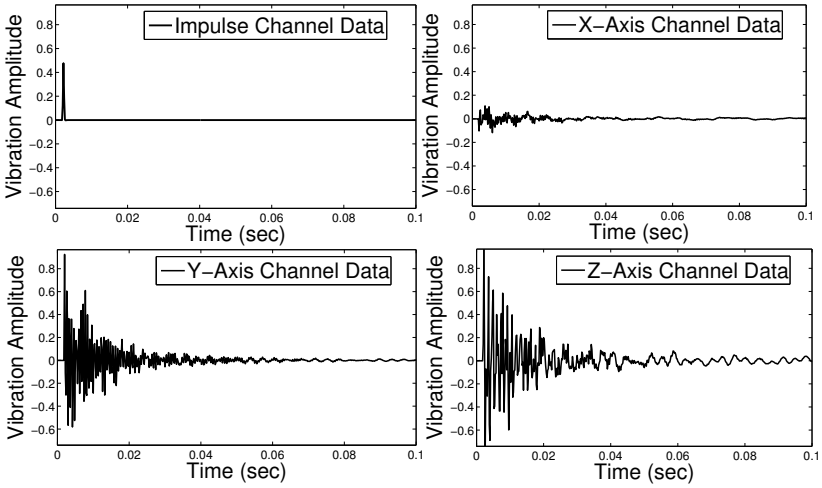

Figure 4.6: A typical time history data obtained by data acquisition system

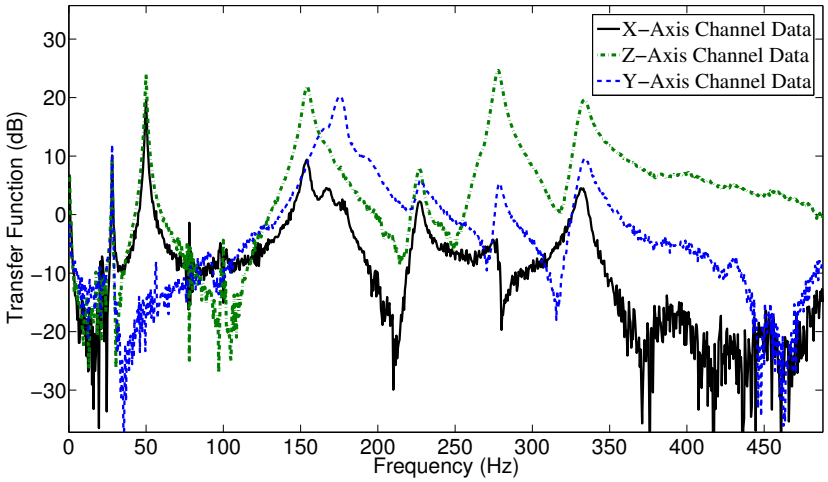

Figure 4.7: A typical frequency response data of Bracket Design-A.

The FRF data is always checked for coherence by repeating the impulse tests for each test configuration. The coherence function, defined as $\gamma^2(\omega) = \frac{|S_{xy(\omega)}|^2}{S_{xx}(\omega)S_{yy}(\omega)}$, is a measure of how well the output $y(t)$ is linearly related to the input $x(t)$. S_{xx} is autocorrelation of the input; S_{yy} is autocorrelation of the output; S_{xy} is cross correlation of the input and the output. A coherence value of 1.0 indicates that the response at that frequency is purely due to the input force and not because of the background noise. Coherence versus frequency curve is generally taken as an indicator of how accurate the measurement process is over a given range of frequencies. Figure 4.8 shows a good coherence at resonance peaks (zero value on a decibel scale) within the frequency range $0-1000$ Hz. However, for the anti-resonances, it is seen that the coherence function dips due to poor signal to noise ratio.

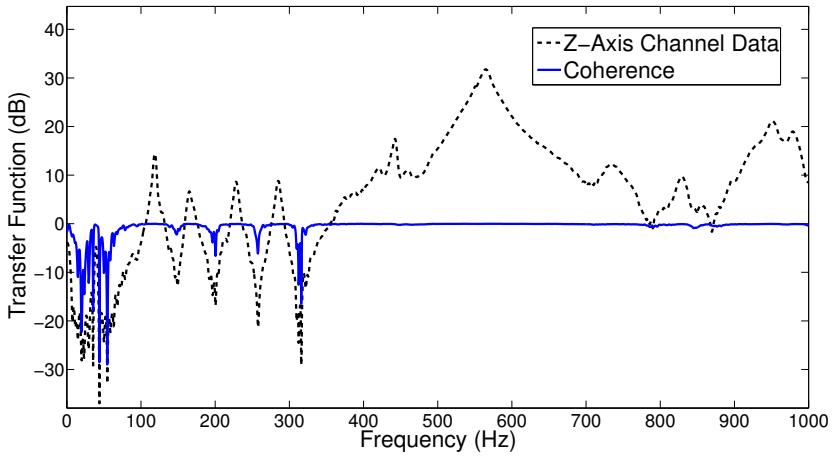

Figure 4.8: A typical frequency response data for one channel with coherence function

Experimentally obtained FRFs within the frequency range $0-500$ Hz for all bracket assemblies are presented in Figures 4.10-4.11. These FRFs are used to identify the natural frequencies and damping ratios associated with each resonance. These modal parameters are obtained by using the system identification methods such as circle fitting and Rational Fraction Polynomial (RFP) method implemented

in the in-house logger software. The results are summarized in Section 4.2.4.

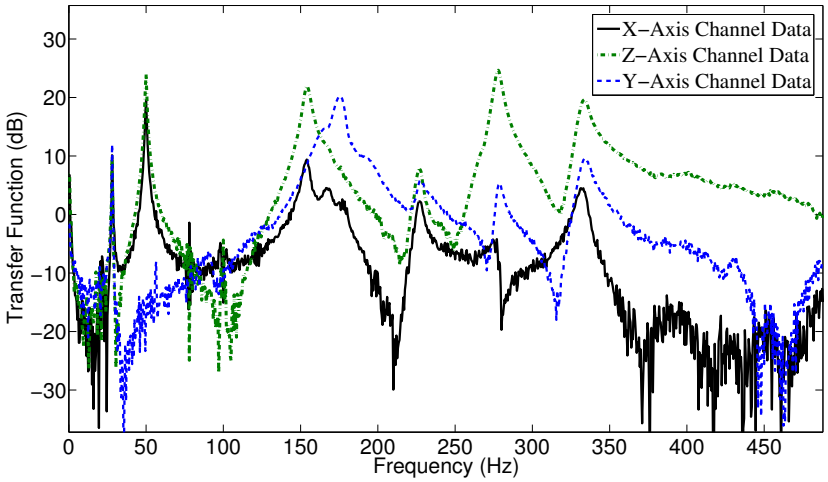

Figure 4.9: FRF for Bracket Design-A

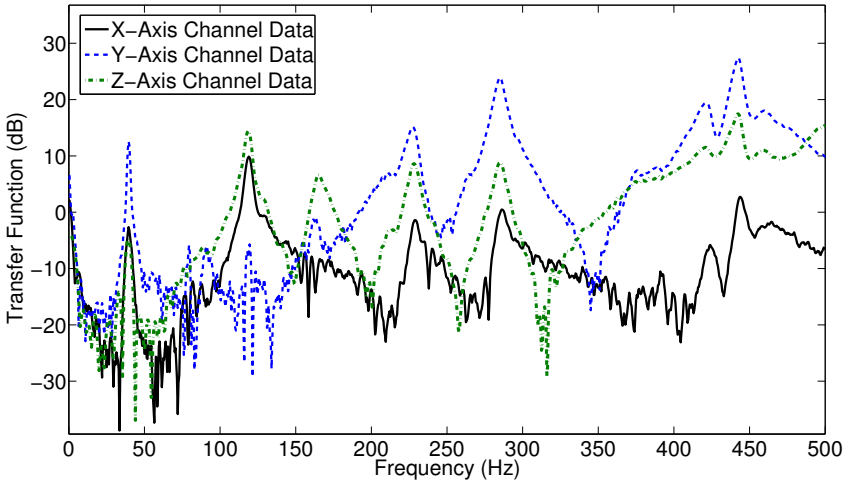

Figure 4.10: FRF for Bracket Design-B

Impulse tests have also been conducted on the wheel. However, a regular hammer was used instead to generate free vibration response. Impulses were applied on the lateral surface of the wheel along the axle direction and also at the circumference of the wheel on the tread to obtain the spectra as shown in Figure 4.12. The

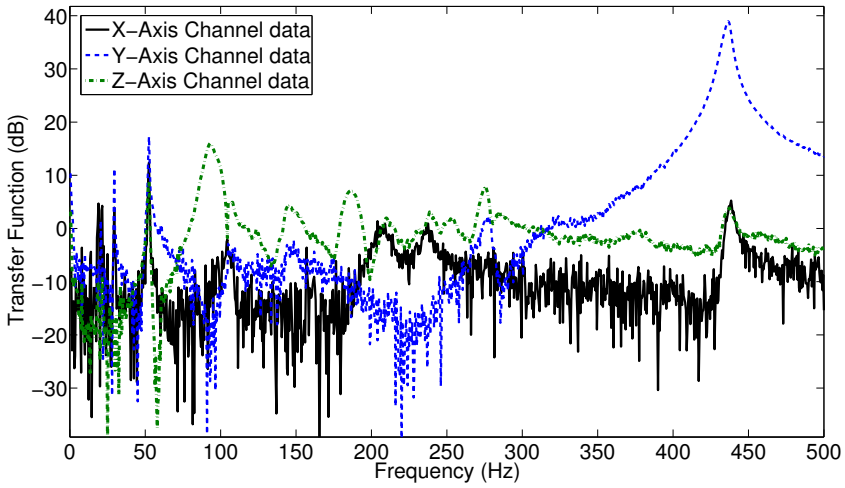

Figure 4.11: FRF for Bracket Design-C

identified natural frequencies are summarised in Section 4.2.4.

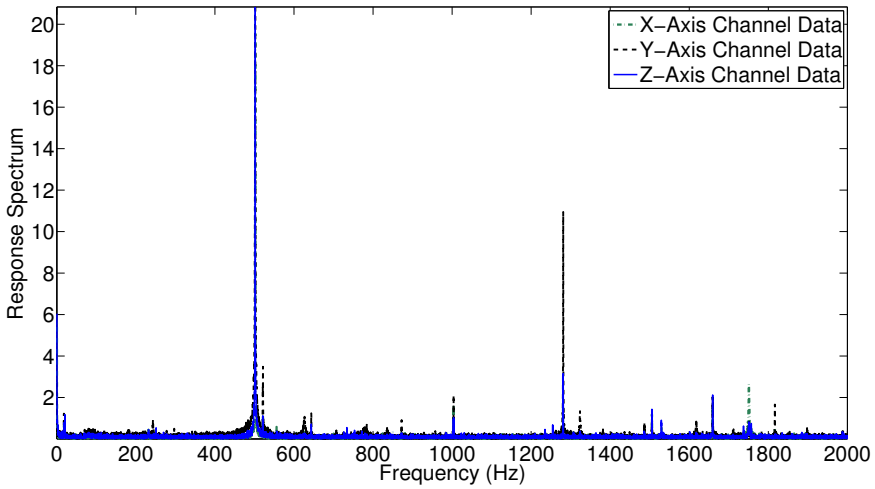

Figure 4.12: Impulse response spectrum for the wheel

4.2.3 Operational Tests

Operating tests were conducted on the FWTR with the stick in contact with a rotating wheel. Figure 4.13 shows a close-up of the stick-wheel interface during one of

the running tests. A microphone is also placed very close to the stick-wheel interface for capturing the generated sounds. A tri-axial accelerometer is placed on top of the applicator near the interface, while another accelerometer is placed on the corresponding bracket. Random noise in the room is recorded even before starting the running test. The driving motor is then switched on and speed is progressively increased from $0-600$ rpm using the operating controls.

Vibration and noise measurements are taken for the increasing rotational speed (run up), steady operating conditions (at maximum speed, roughly 600 rpm) and decreasing rotational speed (run down). It was observed in these tests that most of the vibration is forced vibration type. The data pertaining to these tests is not shown here as no chatter/squeal were observed in the tests.

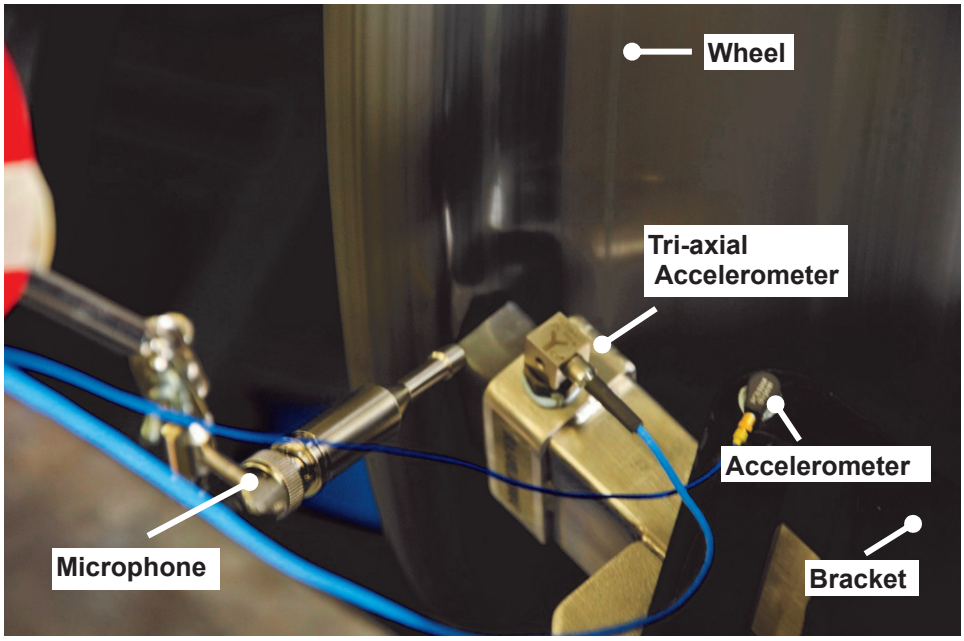

Figure 4.13: Running wheel test

4.2.4 Summary of Measurements

Table 4.1 gives the summary of natural frequencies of the tested bracket designs and the railway wheel.

Table 4.1: Summary of experimentally obtained natural frequencies

Mode No. (n)	Bracket Design-A	Bracket Design-B	Bracket Design-C	Wheel
	Natural frequency, Hz	Natural frequency, Hz	Natural frequency, Hz	Natural frequency, Hz
1	28.2	39.73	29.29	243.5
2	49.9	118.75	52.37	277.66
3	154	167.89	93.82	501.9
4	226.5	227.58	143.55	521.4
5	277	285.17	184.56	1108.91
6	332	421.41	208.81	1280.21
7	645.21	442.91	274.78	1309.02

The experimental data summarized above will be used to validate FE models next.

4.3 Finite Element Modelling

In the design process of friction modifier systems, FE modelling plays an important role to compute FRFs. Given the complexity in geometry, a Computer Aided Design (CAD) package is normally used to generate the geometric features. CAD files generated by SolidWorks^{TM} are imported into ABAQUS/CAE to conduct the FE analysis. The CAD/FE models have already been validated for their physical dimensions and mass by comparing them with the actual components.

4.3.1 Wheel FE Model

The SolidWorks^{TM} models (.*stp files) of the wheel were first imported into ABAQUS for finite element modelling, see Figure 4.14. The axle of the wheel was ignored and clamped boundary conditions were assumed at the inner face of the wheel's

hub. Such an idealization is likely to stiffen the lower modes of the wheel due to flexibility of the axle. The wheel is meshed with solid, homogenous, tetrahedral elements for FE calculations. The Table 4.2 shows the elastic and material properties considered for the wheel.

Table 4.2: Material properties for the railway wheel.

Property	Value
Material	Steel
Density	7850 kg/m^3
Young's Modulus	2.1×10^{11} Pa
Poisson's Ratio	0.3

The frequency analysis step using linear perturbation procedure and Lanczos Eigensolver is then performed in ABAQUS to obtain the natural frequencies and mode-shape amplitudes at the contact point of the wheel with the applicator-bracket assembly. The relevant data is then reported in a text file through ABAQUS which can be used to obtain FRFs using MATLAB©using modal expansion [39].

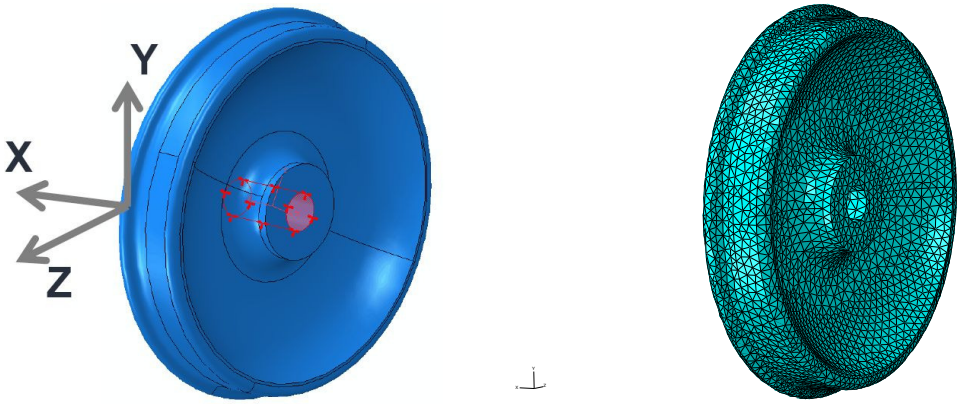

(a) Wheel model in ABAQUS **(b)** Meshed wheel

Figure 4.14: FE analysis of railway wheel

Figure 4.15 depicts a representative set of mode-shapes of the wheel obtained from ABAQUS FE analysis. The wheel mode-shapes shown in Figure 4.15 correspond to one, two, three and four nodal diameter configurations respectively with-

out any nodal circle. In general, the out of plane wheel vibrations can be described by the number of nodal diameters and number of nodal circles. The nodal diameters determine the distribution of vibration amplitudes along the circumferential direction of the wheel, while nodal circles determine the distribution along any radial line. In case of perfect symmetry of railway wheels, nodal lines (nodal diameters) are determined by the excitation point, which is always at the anti-nodal diameter. On the other hand when there are slight imperfections, two distinct modes of each type exist with slightly different natural frequencies. In this case, nodes and anti-nodes are fixed in the structure irrespective of the excitation point.

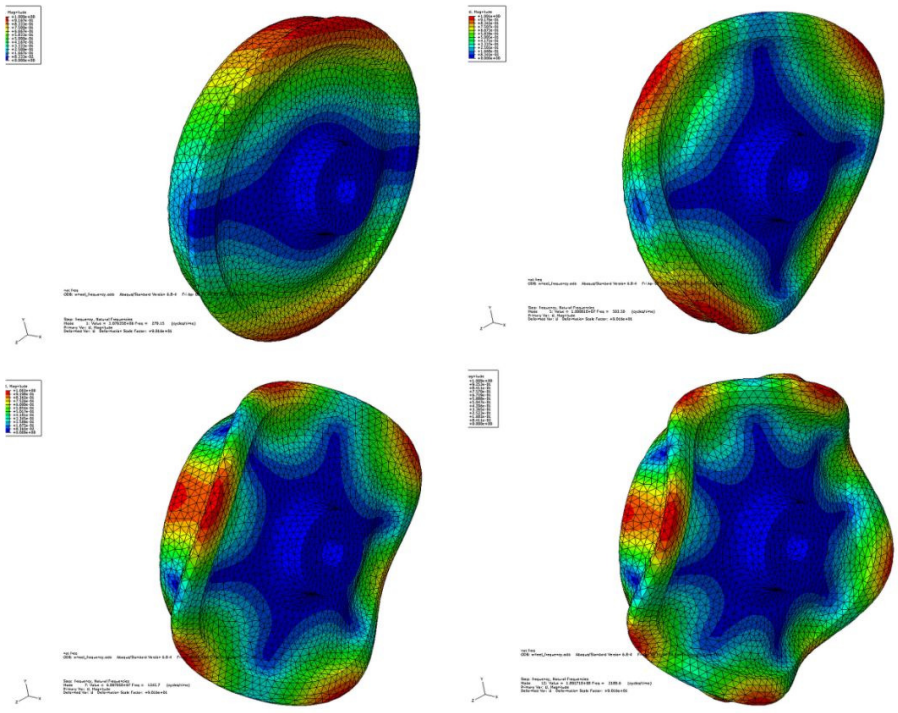

Figure 4.15: Wheel mode-shapes produced by ABAQUS

The computed natural frequencies from FE calculations are summarized in Section 4.3.4. For this numerical analysis, proportional damping was assumed and values of damping parameters were determined through experimental tests.

4.3.2 Applicator-bracket FE Models

While modelling the applicator-bracket assembly the dynamics of the frame are found to be important. The frame of the test-rig is a flexible system in itself. However, modelling the entire frame along with the applicator-bracket is computationally expensive. Reasonably accurate models can be obtained by mounting the applicator-bracket onto the supporting I-beam (rail) in Figure 4.2. Three different modelling configurations can be envisaged: applicator with bracket as shown in Figure 4.16; applicator with bracket mounted on a frame as shown in Figure 4.17; applicator with bracket on a rail as shown in Figure 4.18.

Figure 4.16: FE model of applicator with bracket

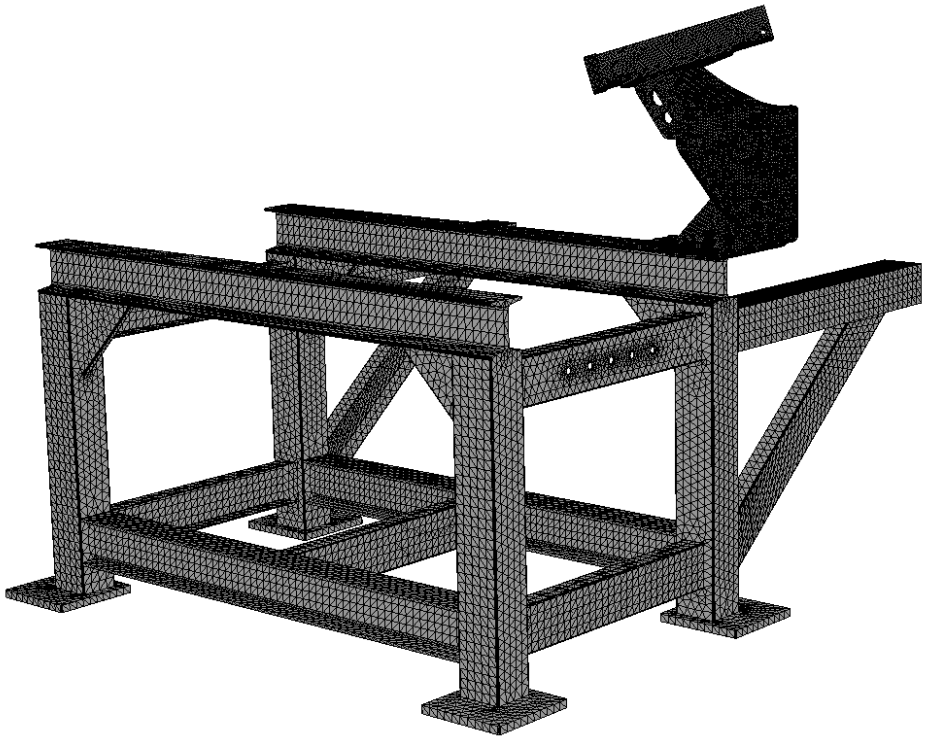

Figure 4.17: FE model of applicator with bracket mounted on a frame

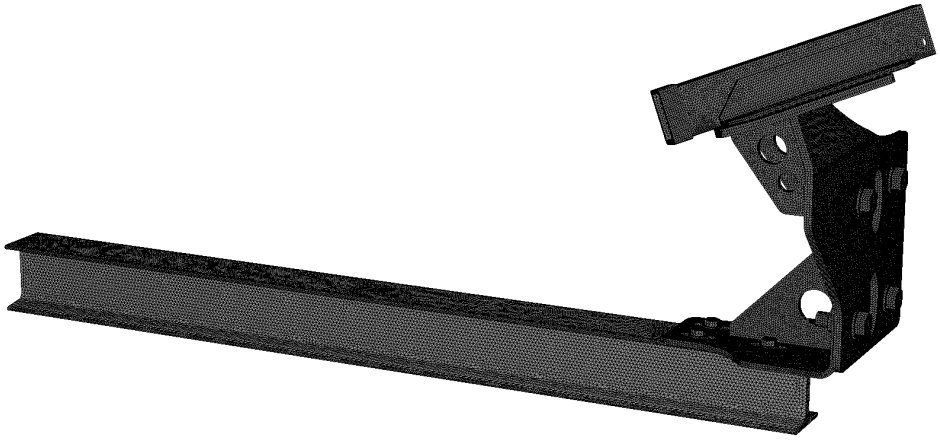

Figure 4.18: FE model of applicator with bracket on the supporting I-beam (rail)

Modelling the applicator with bracket configuration, see Figure 4.16, leads to a stiffer boundary condition at the joint connection with the rail/frame. Evidently, such a configuration shows little resemblance with the experimental numbers for natural frequency. Modelling the whole frame, see Figure 4.17, is computationally expensive. In addition, modelling the driving motor, bearings and axle is cumbersome. It was thus decided to model only the rail instead of the whole frame, see Figure 4.18. The mass of the wheel and motor were lumped onto the rail. The I-beam rail is tied to the supporting bracket using TIE elements. The supporting bracket is again tied to the main bracket and applicator. Encastre boundary conditions were employed on the bottom surface of the I-beam rail in the areas of connection with the frame. Comparison of this model configuration with that of the model having the whole frame, indicated a strong agreement with respect to natural frequencies. Hence, modelling the rail alone is not only computationally efficient, but also a reasonable idealization of the whole frame. We adopt a similar configuration for the other bracket assemblies as well.

Bolts, nuts and washers imported from SolidWorks^{TM} models into ABAQUS were re-designed to suppress the complex features which were difficult to mesh. TIE constraints were used to model the joints at the rail-bracket-applicator interface. Table 4.3 shows the modelling parameters considered for the applicator-bracket assembly. FE simulations have been duly checked for convergence.

Table 4.3: Modelling parameters for applicator-bracket assembly.

Parameters	Values
Material properties (Steel)	Young's Modulus, $E = 2.1\times10^{11}$ Pa Density, $\rho = 7810$ kg/m^3 Poisson's ratio, $\nu = 0.3$
Element type	C3D4, 4-noded linear tetrahedron
Analysis procedure	Linear perturbation, Eigen-solver is Lanczos

Finally natural frequencies and mode-shapes at the desired point are obtained by running the frequency analysis step using the linear perturbation procedure in ABAQUS.

The proportional damping parameters α and β used in the FE analysis of applicator-bracket assembly are derived from the measured damping ratios from the experimentally obtained FRFs. The methodology to obtain these coefficients is explained in the next section.

4.3.3 Proportional Damping Model

A proportional damping model of the form $\mathbf{C} = \alpha\mathbf{M} + \beta\mathbf{K}$ has been assumed for the damping calculations. It gives the relation $2\zeta_n = \frac{\alpha}{\omega_n} + \beta\omega_n$ in the modal domain. By measuring ζ_n and ω_n for several modes, a curve can be fitted using the relation $2\zeta_n = \frac{\alpha}{\omega_n} + \beta\omega_n$ to obtain the parameters α and β.

Measured natural frequencies and Q factor for the first few modes are tabulated in Table 4.4. The damping ratio ζ_n is evaluated from the Q-factors and the corresponding values are plotted against the frequencies as shown in Table 4.5. A curve is fitted on the data points shown in Figure 4.19 yielding the proportional damping coefficients α and β.

Table 4.4: Bracket Design-B: Analysis of FRF data for modal parameters

Mode (n)	Natural frequency (ω_n, Hz)		Damping ratio (ζ_n)		Damping factor Damping factor (Q_n)	
	Mean	S.D.	Mean	S.D.	Mean	S.D.
1	39.73	0.17	0.02472	0.00521	39.73	0.17
2	118.75	0.2	0.01905	0.00084	26.29	1.14
3	167.89	2.21	0.04706	0.01724	11.54	3.79
4	227.58	0.53	0.01742	0.00051	28.73	0.84
5	285.17	0.36	0.01327	0.00176	38.16	4.25
6	421.41	1.38	0.02141	0.00529	24.97	8.26
7	442.91	0.64	0.00825	0.00065	60.95	5.01
8	564.3	1.978	0.02263	0.00821	24.25	7.59

A similar procedure is adopted to obtain the modal damping parameters α and β for the other brackets as well. Table 4.5 gives a list of experimentally obtained

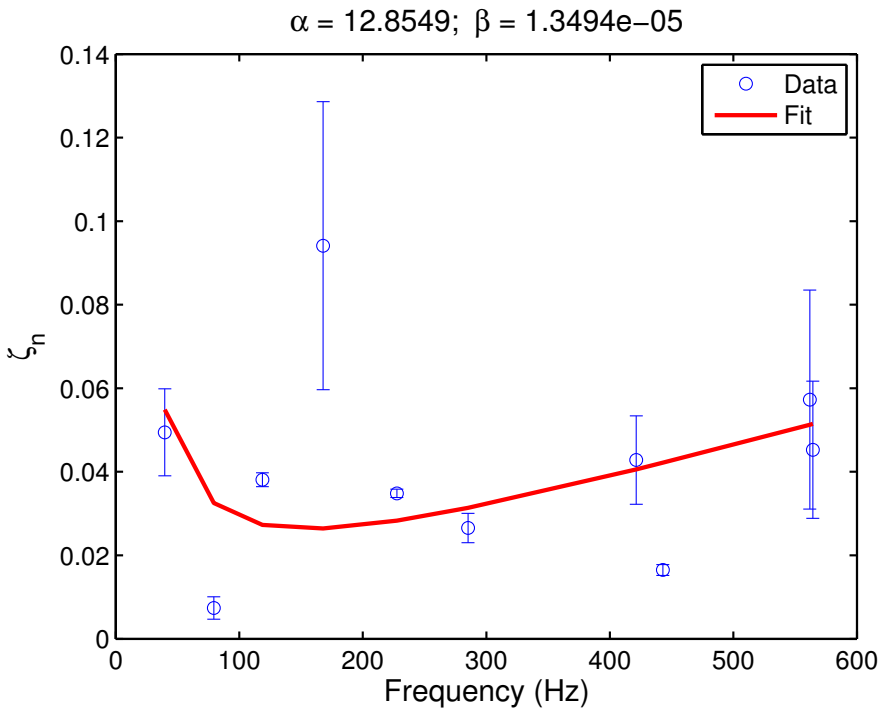

Figure 4.19: Proportional damping model fit $2\zeta_n = \frac{\alpha}{\omega_n} + \beta\omega_n$ for the Bracket Design-B.

proportional damping values for all the sub-systems modelled in FE. It is important to note that non-proportional damping can have a significant influence on the stability. This analysis is beyond the scope of the present work.

Table 4.5: Experimentally determined modal damping parameters α and β

Component	α	β
Bracket Design-A	9.1269	1.8791e-5
Bracket Design-B	12.8549	1.3494e-5
Bracket Design-C	5.4126	5.3259e-6
Railway Wheel	1.310	-1.0737e-10

4.3.4 Summary of FE Modelling

Table 4.6 gives the summary of natural frequencies of the available bracket designs

and the railway wheel, obtained through ABAQUS finite element modelling. It can be observed by comparing the first natural frequencies that the Bracket Design-B is the stiffest configuration of all, followed by Bracket Design-C and Bracket Design-A. It may also be observed that Bracket Design-C has more number of resonant peaks. As will be seen later, this has a significant bearing on the stability maps for Bracket Design-C.

Table 4.6: Summary of FE obtained natural frequencies

Mode No. (n)	Bracket Design-A	Bracket Design-B	Bracket Design-C	Wheel
	Natural frequency, Hz	Natural frequency, Hz	Natural frequency, Hz	Natural frequency, Hz
1	30.976	45.846	37.382	280.57
2	55.358	122.86	54.452	281.08
3	141.22	181.54	86.944	505.15
4	200.58	214.43	169.1	505.78
5	298.95	294.59	194.13	1244.4
6	357.78	414.39	219.38	1245.4
7	467.48	481.29	264.45	1358.9
8	519.71	662.81	315.93	1358.9
9	-	829.75	448.69	-

4.4 Validation of FE Models by Experiments

Table 4.7 presents a comparison of experimental and FE results of the sub-systems. FE modelling results are in reasonable agreement with the experimental measurements.

All the predicted natural frequencies for the three bracket designs are at the most within 10% of experimentally measured values. This is encouraging given the simplifications introduced in the FE modelling as already discussed in Sec-

tion 4.3.2. The FE predictions for the first natural frequency are slightly higher when compared to the measured values. This can be attributed to the frame being simplified as a I-beam rail with encastre boundary conditions and lumped masses for the wheel and the motor; modelling uncertainties in joints. The bearing for the wheel and motor are also not modelled.

As for the wheel, higher measured modes are in better agreement than the first one. This is known and expected since the axle flexibility is ignored and hence the stiffness is overestimated in the FE model. The axle flexibility has little influence on higher modes, see [52] for more details. It is concluded that accurate FE models have been developed.

Table 4.7: Validation of FE model predictions for natural frequencies in Hz with experimental values

Mode (n)	Bracket Design-A		Bracket Design-B		Bracket Design-C		Wheel	
	Exp	F.E	Exp	F.E	Exp	F.E	Exp	F.E
1	28.2	31	39.7	45.9	29.3	37.4	243.5	280.6
2	49.9	55.4	118.8	122.9	52.4	54.4	277.7	281.0
3	154	141.2	167.9	181.5	93.8	87.0	501.9	505.2
4	226.5	200.6	227.6	214.4	143.6	169.1	521.4	505.8
5	277	299	285.2	294.6	184.6	194.1	1108.9	1244.4
6	332	357.8	421.4	414.4	208.8	219.4	1280.2	1245.4
7	645.2	467.5	442.9	481.3	274.8	264.5	1309.0	1358.9
8	-	519.7	564.3	662.8	320.8	315.9	1343.5	1359.4
9	-	-	-	829.8	436.4	448.7	-	-

4.5 Conclusion

In this chapter, experiments conducted on a full wheel test rig for different bracket designs were discussed in detail. Simultaneously, finite element models for the corresponding brackets and railway wheel were developed. FRFs were obtained for

the individual sub-systems by means of experiments. The comparison of natural frequencies obtained by FE calculations corroborated with the measured frequencies on the FWTR.

These validated FE models can now be used to generate the individual sub-system's FRFs entering into the stability criterion Equation 3.8. By assuming a constitutive law for friction forces at the contact the stability comparisons for the three brackets will be made in the next chapter.

Chapter 5

Influence of Bracket Designs on Stability

5.1 Introduction

In Chapter 4, experimentally validated Finite Element (FE) models of the wheel and the bracket-applicator subsystems have been developed. Frequency Response Functions (FRFs) of each subsystem can then be obtained from the FE models using the modal vectors and natural frequencies, provided a suitable damping model based on experimentally measured damping ratios is identified. This allows the computation of the wheel FRFs ($\boldsymbol{G}(\omega)$) and the applicator-bracket FRFs ($\boldsymbol{H}(\omega)$). Once these individual subsystem's FRFs are known, the zeros of the characteristic equation of the closed loop transfer function can be calculated according to Equation 3.8 in Section 3.3, assuming a suitable friction model at the contact. The friction law employed here is Coulomb's fiction rule of the form $F = \mu N$. Since no tribological data related to the friction modifier material is available, the friction coefficient μ is treated as a variable.

Two issues remain to be addressed: wheel rotation and the angle of applicator. Recall that the models developed in Chapter 4 are for a stationary wheel and moreover the angle of applicator α (see Figure 3.1) must also be included. The FRFs for the wheel and the applicator-bracket assembly will be obtained first from the data of validated FE models in Chapter 4. Since the stability of the brackets

need to be compared for a rotating wheel (related to the train speed), wheel FRFs need to be modified. Also, the FRFs of the applicator-bracket model need to be transformed into the local co-ordinates of the contact. This is achieved by using a suitable transformation matrix which depends on the angle of the applicator. These two issues are taken up in Section 5.2.

The variables for a given bracket design that govern the stability according to Equation 3.8 are: coefficient of friction μ, angle of applicator α and speed of train v. The stability hyper surface is multi-dimensional given the number of parameters on which it depends. However, two-dimensional stability maps are readily obtained by fixing one parameter and varying the remaining two. For example, if the angle of applicator α is fixed, then the stability can be visualized as a checkered plot of squares of two colours populating the plane defined by the train speed and the friction coefficient. The black colour denotes instability and the white signifies stability. Such plots are generated for each bracket and for different parameters in Section 5.3 and the three bracket designs are compared. Finally, the results are summarized in the conclusions section in Section 5.5

5.2 Influence of Train Speed and Angle of Applicator

The FRFs for the applicator-bracket assembly ($\boldsymbol{H}$) and the railway wheel ($\boldsymbol{G}$) are shown in Figures 5.1-5.4. These FRFs are for the applicator oriented normal to the stationary wheel. However, the applicator FRFs have to be rotated suitably to account for the angle of applicator and the wheel FRFs have to be corrected to include the effect of rotation.

The influence of train speed/wheel rotation on the FRFs of the wheel and the influence of the angle of applicator on the FRFs of the applicator-bracket systems are now considered in turn.

5.2.1 Influence of Wheel Rotation: Mode Splitting

The railway wheel shown in Figure 4.2 is connected to the axle at the hub. Its cross-section is not uniform due to web profile and presence of the wheel flange. The wheel also loses its perfect symmetry due to manufacturing defects, wear and at times due to re-profiling. We can expect that lack of symmetry will lead to

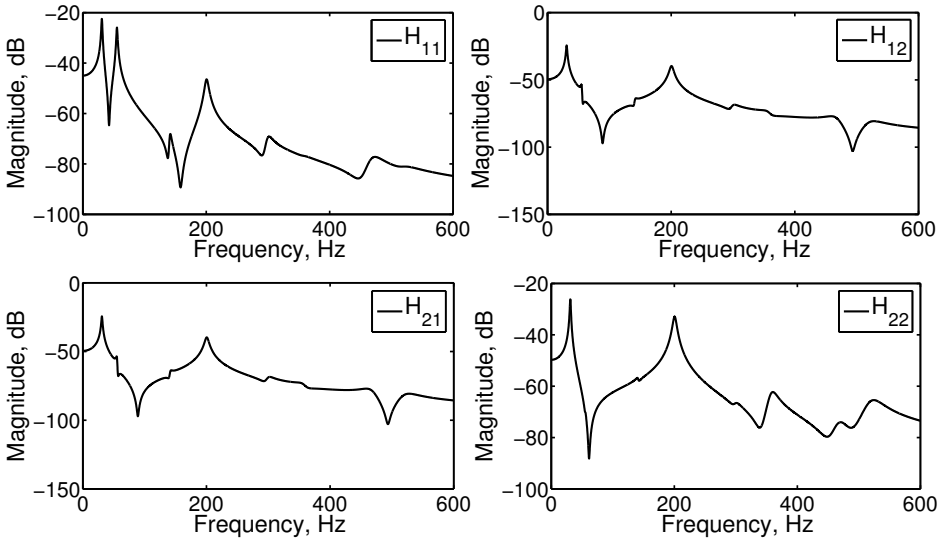

Figure 5.1: Summary of Frequency Response Function matrix, $\boldsymbol{H}$, for Bracket Design – A in the frequency range 0 – 600 Hz

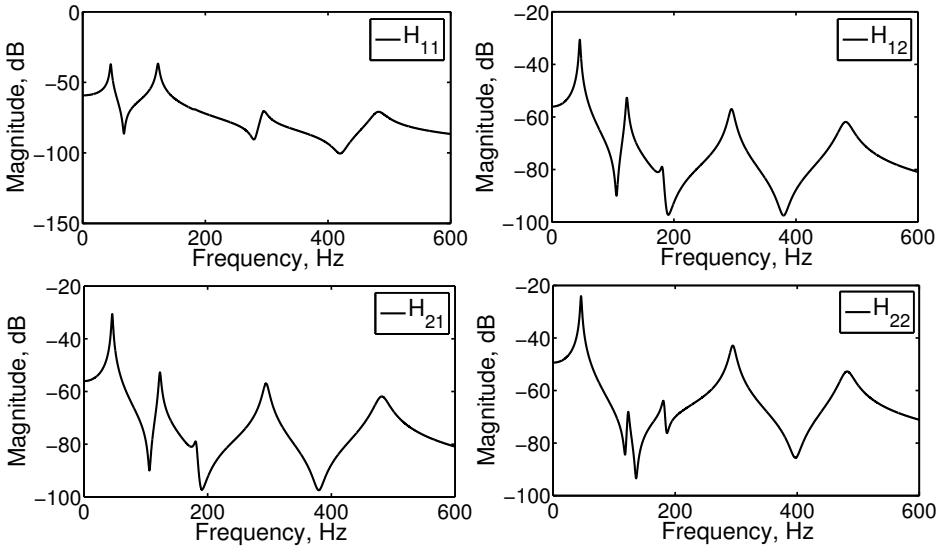

Figure 5.2: Summary of Frequency Response Function matrix, $\boldsymbol{H}$, for Bracket Design – B in the frequency range 0 – 600 Hz

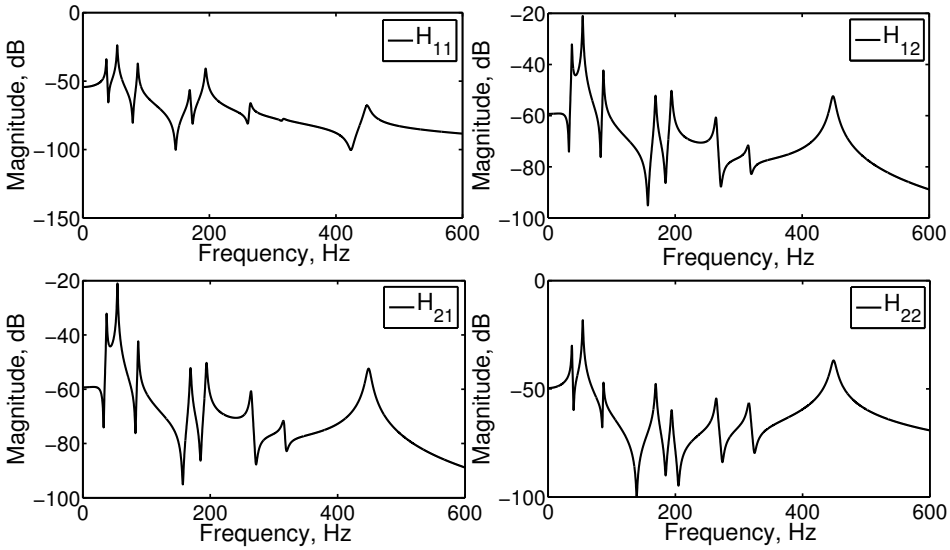

Figure 5.3: Summary of Frequency Response Function matrix, $\boldsymbol{H}$, for Bracket Design – C in the frequency range $0 - 600$ Hz

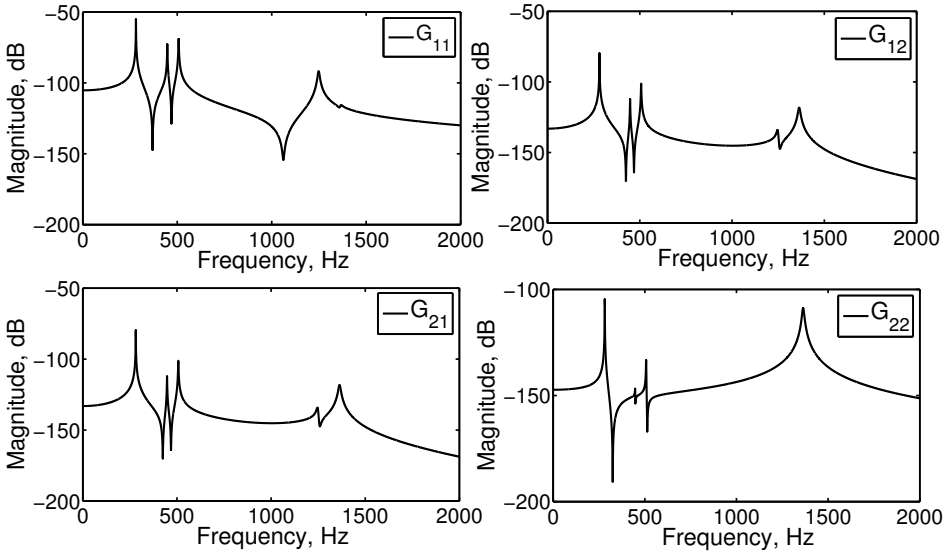

Figure 5.4: Summary of Frequency Response Function matrix, $\boldsymbol{G}$, for railway wheel in the frequency range $0 - 2000$ Hz

splitting of the degenerate modes into two single modes of close and distinct natural frequencies as discussed earlier in Section 2.4.

The FRFs for the stationary wheel can be obtained from the modal parameters computed from the FE model using the following modal expansion [39]:

$$G_{jk}(\omega) = \sum_{r=1}^{N} \frac{\psi_{rj}\psi_{rk}}{m_r(\omega_r^2 - \omega^2 + 2i\zeta_r\omega\omega_r)}, \tag{5.1}$$

where ψ_{rj} and ψ_{rk} denotes mode-shape amplitudes of the r^{th} mode in directions j and k, respectively; m_r is the modal mass for the r^{th} mode. ζ_r is modal damping ratio for the r^{th} mode. This general expression is used to determine the frequency response of a stationary wheel which needs to be modified when a rotating railway wheel is contemplated. There are significant effects on the FRFs owing to the rotation of the wheel as discussed in [55] and Section 2.4. The rotation effects on the wheel FRFs simplify with the following assumptions:

1. Structural effect of rotation such as centrifugal stiffening is neglected.

2. Coriolis forces are neglected which seems a reasonable assumption for the rotation of the wheel corresponding to the typical train speeds.

The wheel FRFs with rotation can be obtained according to (see [55] for derivations)

$$G_{jk}(\omega) = \sum_{m,n} \frac{\psi_{mnj}(r,z)\psi_{mnk}(R,Z)}{2m_{mn}} \left\{ \frac{\varepsilon_{jk}e^{-in\theta_o}}{d_+(\omega)} + \frac{\varepsilon_{jk}^* e^{in\theta_o}}{d_-(\omega)} \right\}, \quad \varepsilon_{jk} = 1, \tag{5.2}$$

where asterisk denotes complex conjugate and $d\pm(\omega)$ is defined as

$$d_\pm(\omega) = \omega_{mn}^2 - (\omega \pm n\Omega)^2 + 2i\zeta_{mn}(\omega \pm n\Omega)\omega_{mn} \tag{5.3}$$

The FRFs after correcting for the speed indicate two resonance peaks for the rotating wheel associated with each natural frequency of the stationary wheel ω_{mn}. Here the subscripts m and n denote the number of nodal circles and nodal diameters respectively. The two new resonances split into $\omega \pm n\Omega$ and the frequency of separation depends on the rotation of the railway wheel (Ω). As for the mode

shape, there isn't a fixed mode-shape, instead we see the occurrence of a single rotating wave. The FRFs of the stationary and rotating wheel are shown in Figure 5.5 for a train speed of 16 km/h, which clearly shows the mode splitting that happens with increasing speed. Note that both these FRFs are based on the FE model for stationary wheel and Equation 5.2.

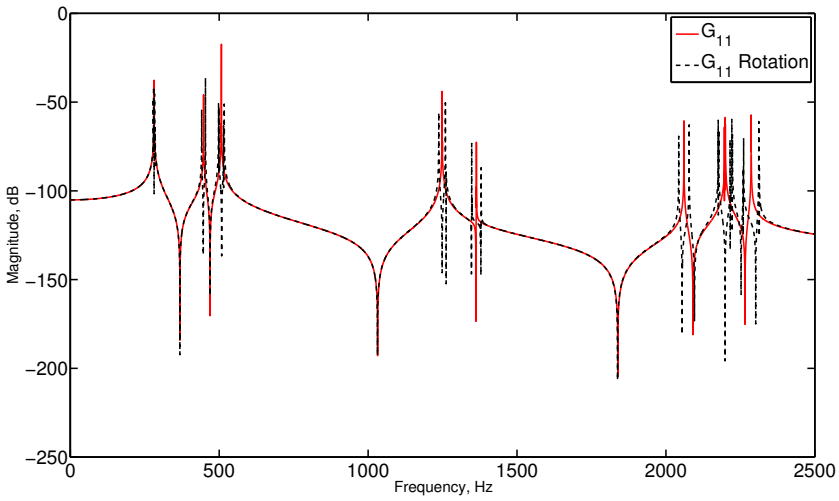

Figure 5.5: Split mode-shapes owing to wheel rotation, corresponding to the train speed of 16 km/h

5.2.2 Orientation of Applicator

The FRFs of the applicator-bracket model need to be transformed into the local co-ordinates of the contact. A coordinate transformation has been implemented on the mode-shapes of the applicator at the contact point to account for various orientations of the applicator. Such a transformation effectively changes the FRFs of the applicator-bracket subsystem. Since characteristic equation is the linear summation of individual frequency response functions of applicator and wheel, pole locations of the closed loop transfer function also change with angle of applicator. Thus, the overall stability of the applicator-bracket-wheel system is influenced by changing the orientation of the applicator. The transformation algorithm is based on the standard Rodrigues's rotation formula (see pp. 164 in [76]) for finite rota-

tions implemented in MATLAB©.

5.3 Stability Diagrams

We have modified the FRFs of the wheel and applicator-bracket assembly considering the effect of the rotation of wheels and the angle of application of sticks respectively. The next step is to determine the stability of the system using these modified FRFs. To proceed with the stability calculations numerically, the mode-shape and natural frequency data, obtained from FE modelling is first exported from ABAQUS in the form of text files. These text files act as an input to the MATLAB©simulation programs.

The FRFs in general, can be represented in two equivalent forms: Pole-Residue Form and Rational Fraction Polynomial (RFP) Form. Rational Fraction Polynomial form of the FRF is expressed as:

$$\begin{aligned} H_{jk} &= \sum_{r=1}^{N} \frac{\psi_{rj}\psi_{rk}}{\omega_r^2 + 2j\zeta_r\omega\omega_r - \omega^2} \\ H_{jk} &= \sum_{r=1}^{N} \frac{0 \times (j\omega)^1 + \psi_{rj}\psi_{rk}(j\omega)^0}{(j\omega)^2 + 2\zeta_r\omega_r \times (j\omega) + \omega_r^2(j\omega)^0} \equiv \frac{N(j\omega)}{D(j\omega)} \end{aligned} \tag{5.4}$$

Note that the above representation of FRF is equivalent to that in Laplace domain, if one inserts Laplace transform variable $s = j\omega$. The resulting expression of RFP form of the FRF is a fraction of two rational polynomials. The natural frequencies are the roots of the denominator polynomial in $s = j\omega$, called poles $s_p = j\omega_p$. The roots of the numerator polynomial $N(s)$ are called zeros. They are frequencies at which the response is zero and hence associated with anti-resonances as mentioned earlier in Section 3.3.2. FRFs of wheel and applicator-bracket assembly can be expressed in the RFP form. Characteristic equation is a linear summation of individual FRFs and thus can also be expressed in a rational fraction form. The roots of the numerator and denominator polynomials of the fraction give the position of zeros and poles, respectively.

In order to obtain the characteristic equation of the closed loop transfer function

in Equation 3.8 which is repeated here

The closed loop system can be unstable if and only if the characteristic equation $D(\omega) = G_{11} + \mu_o G_{12} + H_{11} + \mu_o H_{12}$ has at least one zero in lower half of the complex Fourier plane

the FRFs of individual subsystems: $G(\omega)$ and $H(\omega)$ are first obtained as a fraction of two rational polynomials by convolving the corresponding numerator and denominator of the summation components in the RFP expression given by Equation 5.4. The roots of the numerator and denominator polynomial functions give the zeros and poles of the individual subsystems respectively. The FRFs of the wheel and the applicator-bracket assembly are of stable systems. Hence, the poles should lie in the upper half of the complex Fourier plane as shown in Figure 5.6.

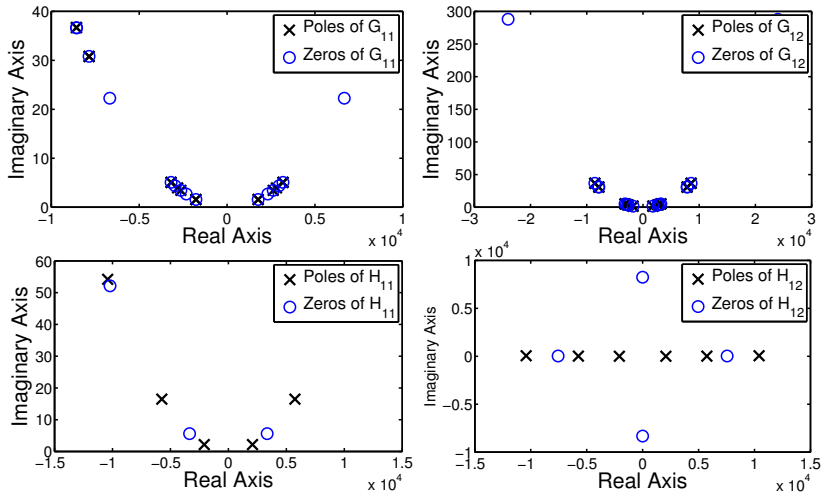

Figure 5.6: The plot shows poles and zeros for individual transfer functions for a typical case

Referring to the characteristic equation Equation 5.3, we now have FRFs in rational fraction form. Thus, characteristic equation can now be expressed as a summation of FRFs in rational fraction form:

$$Ch.Equation = \frac{Num(G_{11})}{Den(G_{11})} + \mu_o \frac{Num(G_{12})}{Den(G_{12})} + \frac{Num(H_{11})}{Den(H_{11})} + \mu_o \frac{Num(H_{12})}{Den(H_{12})} \quad (5.5)$$

We convolve the respective numerator and denominator to obtain the numerator and denominator of the characteristic equation i.e., numerator of the characteristic equation is obtained by evaluating corresponding terms for each fraction such as: $Num(G_{11}) * Den(G_{12}) * Den(H_{11}) * Den(H_{12})$ and finally adding them. On the other hand, the denominator is obtained by evaluating $Den(G_{11}) * Den(G_{12}) * Den(H_{11}) * Den(H_{12})$.

Finally, we have obtained the numerator and denominator polynomial of the characteristic equation. Stability is now judged based on the roots of the numerator polynomial of the characteristic equation. For a stable case, zeros of the numerator polynomial should lie in the upper half of the Fourier domain or in the left half plane of the Laplace domain. A typical unstable system is shown in Figure 5.7, where some zeros (shown as dark circles) of the characteristic equation lie in the lower half complex Fourier plane.

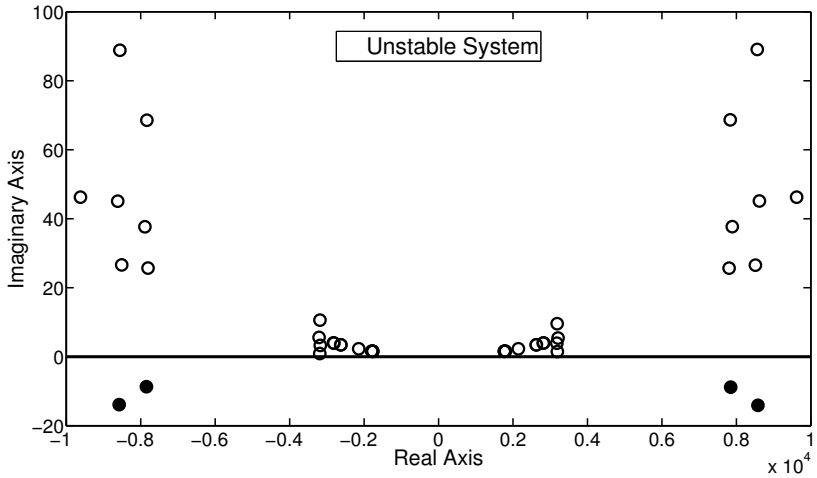

Figure 5.7: Plot shows a typical unstable system, wherein the zeros indicated as dark circles are also present in the lower half of the complex plane, indicating instability

Based on the above procedures, stability diagrams are obtained for parameters of interest to this study. The variables for a given bracket design that govern the stability according to Equation 3.8 are: coefficient of friction μ, angle of applicator α (through the co-ordinate transformations of $\boldsymbol{H}$) and speed of train v. Two-

dimensional stability diagrams are obtained by fixing one parameter and varying the remaining two. For example, if the train speed is fixed, then the stability can be visualized as a checkered plot of squares of two colours populating the plane defined by the angle of applicator α and the friction coefficient. For a particular set of parameters, the zeros of $D(\omega)$ in Equation 5.3 make the overall system stable or unstable. The stability diagrams are obtained by varying the parameters of interest within a reasonable range.

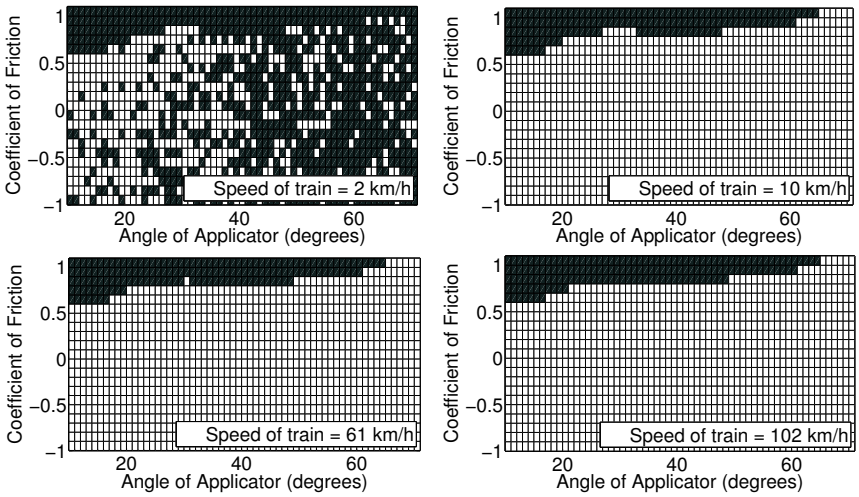

Figure 5.8: Stability diagram for Bracket Design–A: angle of applicator versus coefficient of friction for different train speeds

Figure 5.8 is a checkered plot for Bracket Design-A assembly showing different combinations of angle of applicator and coefficient of friction at different train speeds. It is evident from the graph that as we increase the speed of the train, the density of white blocks increases, indicating higher stability at higher train speeds. Such a feature is also confirmed in practice, as it is observed that squeal sound is prominent at lower speeds and ceases to occur at higher train speeds. It is also interesting to note that, for high values of coefficient of friction, increase in speed of train doesn't necessarily stabilize the system. Such behaviour is noticed on field when the track and wheel are rough, either due to rusting or due to the presence of contaminants. The system incurs squeal sounds at most speeds. When a new train or track is introduced in operation, the coefficient of friction on the interface

is generally high and we encounter such situations.

Figure 5.9 shows a stability diagram for Bracket Design–A assembly, plotted between the angle of applicator versus speed of the train at coefficient of friction values of 0.1. The system is mostly unstable for any orientation of applicator for low speeds. But as the speed of the train increases, stability is regained.

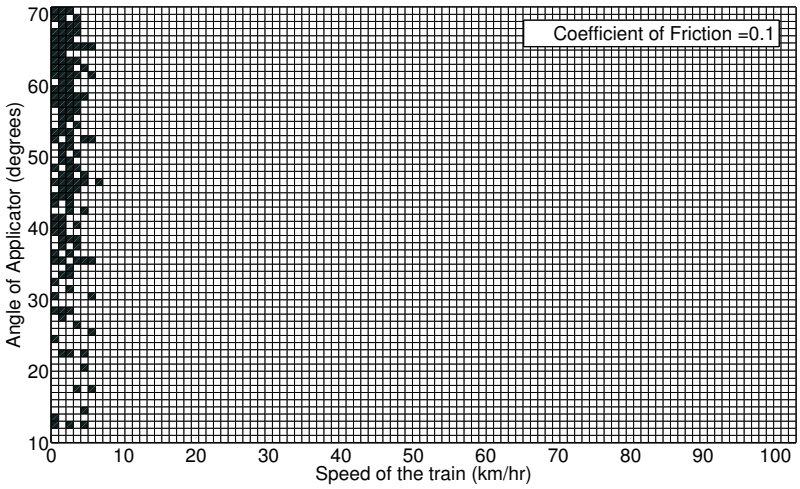

Figure 5.9: Stability diagram for Bracket Design–A: angle of applicator versus train speed

Figure 5.10 shows a stability diagram for Bracket Design–A assembly, plotted between the coefficient of friction versus speed of the train for a particular angle of applicator of value 30 degrees. The diagram indicates stability at higher train speeds. Again, the plot shows that for high values of coefficient of friction, increase in the speed of the train does not stabilize the system.

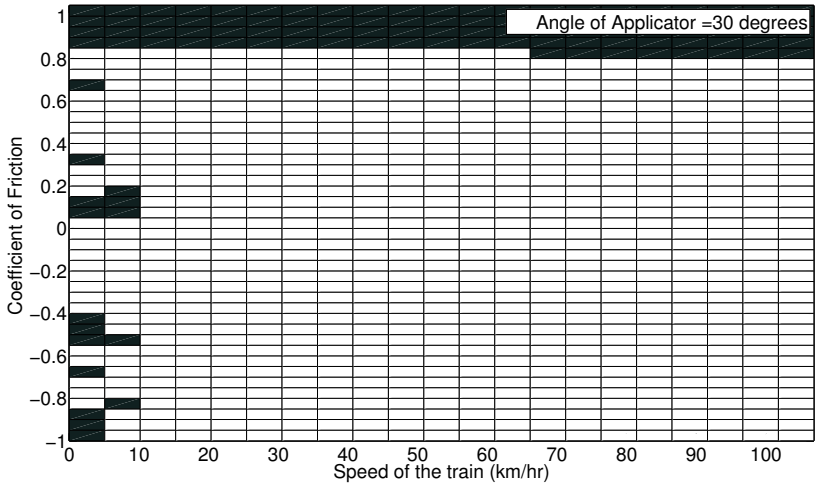

Figure 5.10: Stability diagram for Bracket Design–A: coefficient of friction versus train speed

5.4 Comparison of Bracket Designs

This section gives a relative comparison of stability characteristics of all the three available bracket designs. Figures 5.11-5.13 show different combinations of angle of applicator and coefficient of friction at different train speeds for Bracket Designs-A, B and C respectively.

Using the same applicator and similar mounting configurations, we compare the three bracket designs qualitatively by looking at the stability plots. Bracket Design-B looks to be the most stable bracket with maximum white regions, followed by Bracket Design-A while Bracket Design-C is the least stable of all. It is noteworthy to see that Bracket Design-C has some islands of stability, while instability exists for the rest of the parametric space.

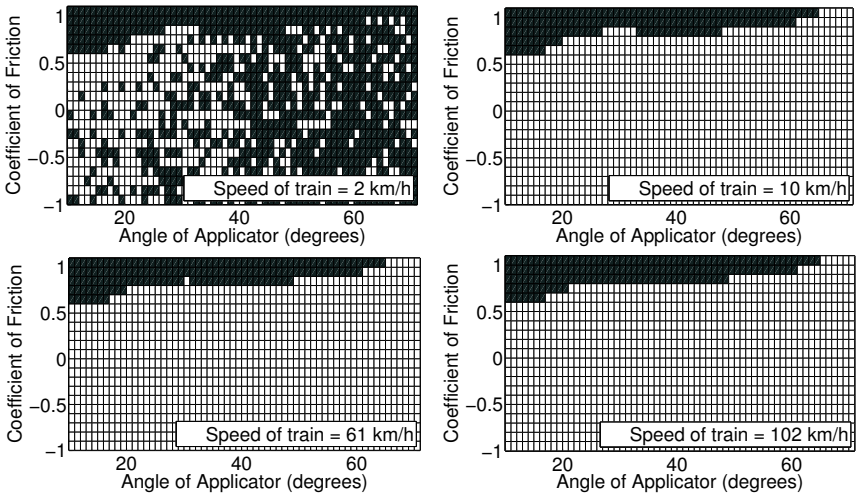

Figure 5.11: Stability diagram for Bracket Design–A: angle of applicator versus coefficient of friction at several train speeds

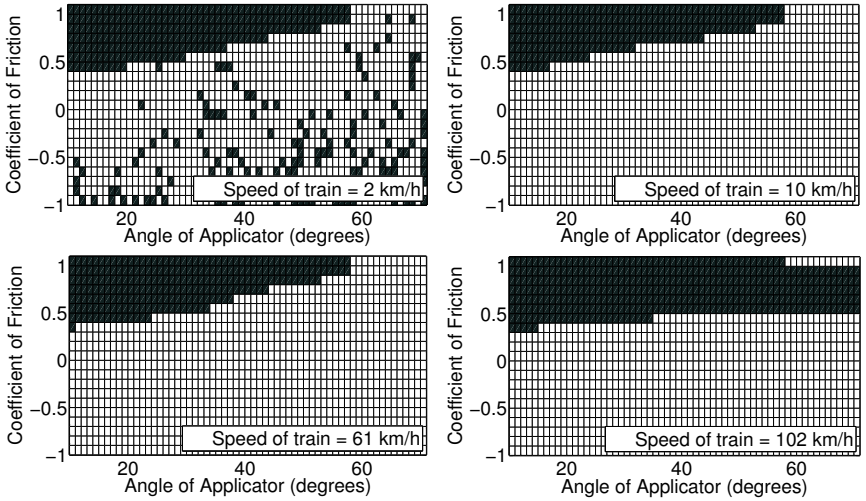

Figure 5.12: Stability diagram for Bracket Design–B: angle of applicator versus coefficient of friction for different train speeds

5.5 Conclusion

This chapter focusses on obtaining the stability diagrams for three parameters of interest: Coefficient of friction, angle of applicator and speed of the train. The

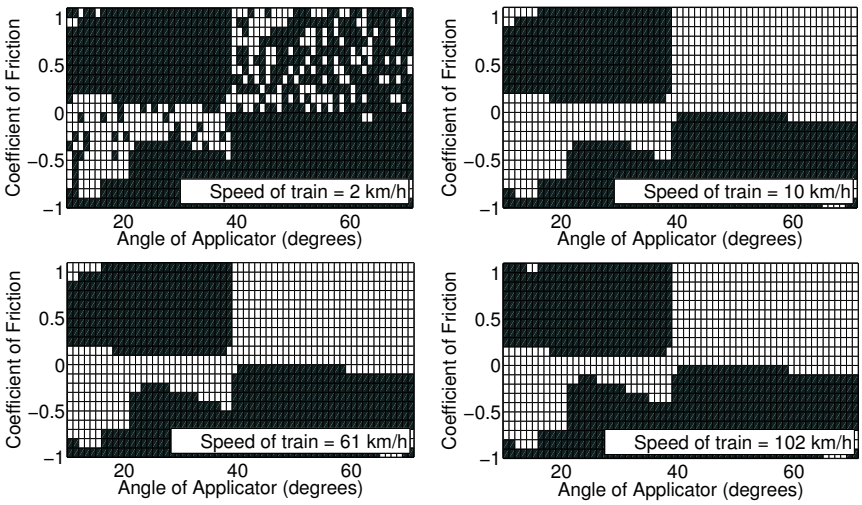

Figure 5.13: Stability diagram for Bracket Design–C: angle of applicator versus coefficient of friction for different train speeds

influence of rotation of the railway wheel is incorporated for the estimation of wheel transfer functions. This allows the train speed to be one of the parameters for determining the stability regions. On the other hand, a coordinate transformation is applied on the applicator-bracket assembly transfer function at the contact point to take into account, the angle of application of the sticks. The stability diagrams in the form of chequered plots are obtained by varying the parameters of interest within a reasonable range. Finally, a relative comparison of stability is undertaken for all the studied bracket designs. Bracket Design-B is found to be the most stable bracket, followed by Bracket Design-A while Bracket Design-C is the least stable of all the designs.

Chapter 6

Conclusions

The principal objective of this dissertation was to develop a stability prediction methodology that can be used by designers of solid stick friction modifier systems in Railway industry. Towards this end, a stability criterion was established based on the transfer functions of individual subsystems and a contact friction model assuming constant coefficient of friction in Chapter 3. The dynamics of both subsystems: wheel and applicator are captured through their corresponding frequency response function (FRF) matrices evaluated at the point of contact. Experimentally validated Finite Element models are developed for three bracket designs in Chapter 4. Corrections to the wheel FRFs due to rotation were incorporated in Chapter 5. This allows the speed of the train to be included as one of the parameters for determining the stability regions. The wheel FRF matrices can change owing to the changes in the speed of the train, while the applicator transfer function change with changes in the orientation of the applicator relative to the wheel. Any changes in the design of the bracket assembly also influence the applicator FRF matrices. In addition, contact conditions at the stick-wheel interface are complex with regards to determining a value for the friction coefficient. Hence, the coefficient of friction is considered as a *variable*. The applicator and the wheel FRFs along with a velocity independent coefficient of friction are then used to generate the closed-loop transfer function and finally the stability is assessed by observing the location of the CLTF's poles. Stability characteristics of three bracket designs have been compared in Chapter 5 using checkered plots.

The main conclusions emanating from this research are summarised next followed by suggestions for future work.

6.1 Contribution of This Dissertation

1. A frequency domain stability analysis procedure is developed and applied to compare the stability characteristics of three bracket designs of solid stick friction modifier systems.

2. The stability of friction modifier systems was found to depend on the following design parameters: Speed of the train, coefficient of friction and angle of applicator with respect to the wheel.

3. Overall, increasing train speeds improves stability for low coefficient of friction conditions. However, at higher coefficients of friction, increase in the speed of the train does not necessarily stabilize the system.

4. A qualitative stability comparison of available bracket designs is undertaken assuming constant coefficient of friction conditions for the contact. For the same applicator and similar mounting configurations, Bracket Design-B assembly is found to be the most stable followed by Bracket Design-A. Bracket Design-C was found to be the least stable bracket design, possibly due to the presence of a high number of resonant modes within 500 Hz.

5. The major advantage of using the transfer function approach is the fact that it is model independent and is measurable. Therefore, any design change can be easily incorporated by the proposed methodology and comparisons can be made between several designs.

6.2 Suggestions for Further Research

1. This work employs a very simple velocity independent friction rule. This was necessary, given the available data on the tribological characteristics of the friction modifier material. It is assumed that the coefficient of friction

is constant over the whole train speed range. However in reality, velocity dependent friction is possible. Incorporating velocity-dependence in the friction law is one direction for further work.

2. The limitation of using frequency domain modelling approach is that the stability is assessed from a steady operating condition. So we miss any instabilities that may arise from the transient vibrations. Thus, a time domain based analysis is imperative in future for capturing the complete dynamics of the system.

3. In this research, we have developed a first order wheel-applicator-bracket model ignoring any contact stiffness and damping in the friction contact model. Contact stiffness and damping parameters are still unknown and need to be determined only through tribological tests. Thus, inclusion of contact parameters in the friction contact model would be a part of future work.

4. In the modelling, we have assumed free boundary conditions at the circumference of the wheel. But in practice, railway wheel is always in contact with the rail. Inclusion of rail-wheel contact would essentially change the transfer function for the wheel sub-system and in turn, change the overall stability of the system. Introduction of rail-wheel contact in the model is necessarily a part of future work.

The long term goal of this research is to develop a stability prediction software which would help designers to design applicator-brackets and compare their stability patterns in a virtual environment. This will lead to structurally robust friction control systems while reducing noise and wear problems emanating from the rail-wheel contact.

Bibliography

[1] Anderson, R., Elkins, J. A., Brickle, B. V., Aref, H., and Phillips, J. W., 2002. *Rail Vehicle Dynamics for the 21st Century*. Springer Netherlands, pp. 113–126. → pages 1

[2] Chiddick, K., and Eadie, D., 1999. "Wheel/ rail friction management solutions". *ProRail 1999*. → pages 1, 14, 15

[3] Dawson, G., April 1911. "Flange lubricating device". *US Patent 990637*. → pages 4, 5

[4] Eadie, D., and Hui, R., 2004. "Wheel life extension with on-board solid stick flange lubrication". *14th International Wheelset Congress.* → pages 7

[5] Popp, K., and Stelter, P., 1990. "Stick-slip vibrations and chaos". *Philosophical Transactions: Physical Sciences and Engineering,* **332**, pp. 89–105. → pages 9

[6] Butlin, T., and Woodhouse, J., 2010. "Friction induced vibration: Quantifying sensitivity and uncertainty". *Journal of Sound and Vibration,* **329**, pp. 509–526. → pages 9, 19, 20

[7] Armstrong-Helouvry, B., 1994. "A survey of models, analysis tools and compensation methods for the control of machines with friction". *Automatica,* **30**(7), pp. 1083 – 1138. → pages 9, 11, 16

[8] Armstrong-Helouvry, B., 1990. "Stick-slip arising from stribeck friction". *IEEE International Conference on,* **2**, pp. 1377–1382. → pages 12

[9] Carter, F., 1926. "On the action of a locomotive driving wheel". *Proc. R. Soc. Lond. A,* **112**, pp. 151–157. → pages 11

[10] Johnon, K., 2008. "An experimental study of creepage in rolling contact". *Symposium of Advances in Contact Mechanics: a tribute to Prof. J.J. Kalker*. → pages 11

[11] Iwnicki, S., 2006. *Handbook of Railway Vehicle Dynamics*. CRC Press. → pages 13, 14

[12] Wickens, A., 1965. "The dynamic stability of railway vehicle wheelsets and bogies having profiled wheels". *International Journal of Solids and Structures,* **1**(3), pp. 319 – 341. → pages 11

[13] Eadie, D., Kalousek, J., and Chiddick, K., 2002. "The role of high positive friction (hpf) modifier in the control of short pitch corrugations and related phenomena". *Wear,* **253**(1-2), pp. 185 – 192. → pages 12

[14] Canudas-de Wit, C., Tsiotras, P., Velenis, E., Basset, M., and Gissinger, G., 2003. "Dynamic friction models for road/tire longitudinal interaction". *Vehicle System Dynamics,* **39**. → pages 16

[15] Ibrahim, R., 1994. "Friction-induced vibration, chatter, squeal, and chaos—part i: Mechanics of contact and friction". *Applied Mechanics Reviews,* **47**(7), pp. 209–226. → pages 16

[16] Ibrahim, R., 1994. "Friction-induced vibration, chatter, squeal, and chaos—part ii: Dynamics and modeling". *Applied Mechanics Reviews,* **47**(7), pp. 227–253. → pages 16

[17] Rabinowicz, E., 1965. *Friction and wear of materials*. Wiley New York. → pages 16

[18] Feeny, B., Ardéshir, G., Hinrichs, N., and Popp, K., 1998. "A historical review on dry friction and stick-slip phenomena". *Applied Mechanics Reviews,* **51**(5), pp. 321–341. → pages 16

[19] Akay, A., 2002. "Acoustics of friction". *The Journal of the Acoustical Society of America,* **111**(4), pp. 1525–1548. → pages 16

[20] Brockley, C., and Davis, H., 1968. "The time-dependence of static friction". *Journal of Lubrication Technology*, pp. 35–41. → pages 17

[21] Rabinowicz, E., 1958. "The intrinsic variables affecting the stick-slip process". *Proceedings of the Physical Society,* **71**(4), p. 668. → pages 17

[22] Brockley, C., Cameron, R., and Potter, A., 1967. "Friction-induced vibration". *ASME J. Lubr. Technol,* **89**(2), pp. 101–108. → pages 17

[23] Yokoi, M., and Nakai, M., 1979. "A fundamental study on frictional noise : 1st report, the generating mechanism of rubbing noise and squeal noise". *Bulletin of JSME,* **22**(173), pp. 1665–1671. → pages 17

[24] Yokoi, M., and Nakai, M., 1980-12. “A fundamental study on frictional noise : 2nd report, the generating mechanism of squeal noise of higher modes”. *Bulletin of JSME,* **23**(186), pp. 2118–2124. → pages

[25] Yokoi, M., and Nakai, M., 1981-08. “A fundamental study on frictional noise : 3rd report, the influence of periodic surface roughness on frictional noise”. *Bulletin of JSME,* **24**(194), pp. 1470–1476. → pages

[26] Yokoi, M., and Nakai, M., 1981-08. “A fundamental study on frictional noise : 4th report, the influence of angle of inclination of the rod on frictional noise”. *Bulletin of JSME,* **24**(194), pp. 1477–1483. → pages

[27] Yokoi, M., and Nakai, M., 1982-05. “A fundamental study on frictional noise : 5th report, the influence of random surface roughness on frictional noise”. *Bulletin of JSME,* **25**(203), pp. 827–833. → pages 17

[28] Chen, G., and Zhou, Z. R., 2003. “Correlation of a negative friction-velocity slope with squeal generation under reciprocating sliding conditions”. *Wear,* **255**(1-6), pp. 376 – 384. 14th International Conference on Wear of Materials. → pages 18

[29] Jarvis, R., and Mills, B., 1963. “Vibrations induced by dry friction”. *ARCHIVE: Proceedings of the Institution of Mechanical Engineers 1847-1982 (vols 1-196),* **178**(1963), pp. 847–866. → pages 18, 19, 20

[30] Earles, S., and Lee, C., 1976. “Instabilities arising from the frictional interaction of a pin-disc system resulting in noise generation.”. *Transactions of the American Society of Mechanical Engineers, Journal of Engineering for the Industry,* **98**. → pages 19

[31] Papinniemi, A., Lai, J., Zhao, J., and Loader, L., 2002. “Brake squeal: a literature review”. *Applied Acoustics,* **63**(4), pp. 391 – 400. → pages 19

[32] Kinkaid, N., O’Reilly, O. M., and Papadopoulos, P., 2003. “Automotive disc brake squeal”. *Journal of Sound and Vibration,* **267**(1), pp. 105 – 166. → pages

[33] Ouyang, H., Nack, W., Yuan, Y., and Chen, F., 2005. “Numerical analysis of automotive disc brake squeal: a review”. *International Journal of Vehicle Noise and Vibration,* **1**, pp. 207 – 231. → pages

[34] Ouyang, H., Mottershead, J. E., Brookfield, D. J., James, S., and Cartmell, M. P., 2000. “A methodology for the determination of dynamic instabilities in a car disc brake”. *international Journal of Vehicle design,* **23**. → pages

[35] Ouyang, H., Mottershead, J. E., and Li, W., 2003. "A moving-load model for disc-brake stability analysis". *Journal of Vibration and Acoustics,* **125**(1), pp. 53–58. → pages 19

[36] Duffour, P., and Woodhouse, J., 2004. "Instability of systems with a frictional point contact. part 1: basic modelling". *Journal of Sound and Vibration,* **271**(1-2), pp. 365 – 390. → pages 19, 34

[37] Duffour, P., and Woodhouse, J., 2004. "Instability of systems with a frictional point contact. part 2: model extensions". *Journal of Sound and Vibration,* **271**(1-2), pp. 391 – 410. → pages

[38] Duffour, P., and Woodhouse, J., 2007. "Instability of systems with a frictional point contact–part 3: Experimental tests". *Journal of Sound and Vibration,* **304**(1-2), pp. 186 – 200. → pages 19

[39] Ewins, D., 1995. *Modal testing: Theory and practice*. Research Studies Press (Taunton, Somerset, England and New York). → pages 19, 58, 72

[40] Hemsworth, B., 1979. "Recent developments in wheel/rail noise research". *Journal of Sound and Vibration,* **66**(3), pp. 297 – 310. → pages 20

[41] ten Wolde, T., and van Ruitten, C., 1983. "Sources and mechanisms of wheel/rail noise: state-of-the-art and recent research". *Journal of Sound and Vibration,* **87**(2), pp. 147 – 160. → pages 21

[42] Bender, E., and Remington, P., 1974. "The influence of rails on train noise". *Journal of Sound and Vibration,* **37**(3), pp. 321 – 334. → pages 21

[43] Remington, P., 1976. "Wheel/rail noise– part i: Characterization of the wheel/rail dynamic system". *Journal of Sound and Vibration,* **46**(3), pp. 359 – 379. → pages 21

[44] Remington, P., 1976. "Wheel/rail noise–part iv: Rolling noise". *Journal of Sound and Vibration,* **46**(3), pp. 419 – 436. → pages

[45] Remington, P., 1987. "Wheel/rail rolling noise, i: Theoretical analysis". *Journal of the Acoustical Society of America,* **81**, pp. 1805–1823. → pages 21

[46] Thompson, D., Hemsworth, B., and Vincent, N., 1996. "Experimental validation of the twins prediction program for rolling noise, part 1: Description of the model and method". *Journal of Sound and Vibration,* **193**(1), pp. 123 – 135. → pages 21

[47] Dings, P., and Dittrich, M. G., 1996. "Roughness on dutch railway wheels and rails". *Journal of Sound and Vibration,* **193**(1), pp. 103 – 112. → pages 21

[48] Sato, S., and Matsuhisa, H., 1978-10. "Study on the mechanism of train noise and its countermeasure : Part i; characteristics of wheel vibration". *Bulletin of JSME,* **21**(160), pp. 1475–1481. → pages 21

[49] Matsuhisa, H., and Sato, S., 1979-11. "Study on the mechanism of train noise and its countermeasures : Partii, the effect of velocity and load, and the characteristics of sound radiation". *Bulletin of JSME,* **22**(173), pp. 1626–1631. → pages 21

[50] Matsuhisa, H., Honda, Y., and Sato, S., 1981-05. "Study on the mechanism of train noise and its countermeasure : Part iii, wheel flexural vibration including the effects of shear deformation and rotatory inertia". *Bulletin of JSME,* **24**(191), pp. 849–853. → pages 22

[51] Thompson, D., 1993. "Wheel-rail noise generation, part i: Introduction and interaction model". *Journal of Sound and Vibration,* **161**(3), pp. 387 – 400. → pages 22

[52] Thompson, D., 1993. "Wheel-rail noise generation, part ii: Wheel vibration". *Journal of Sound and Vibration,* **161**(3), pp. 401 – 419. → pages 66

[53] Thompson, D., 1993. "Wheel-rail noise generation, part iii: Rail vibration". *Journal of Sound and Vibration,* **161**(3), pp. 421 – 446. → pages

[54] Thompson, D., 1993. "Wheel-rail noise generation, part iv: Contact zone and results". *Journal of Sound and Vibration,* **161**(3), pp. 447 – 466. → pages

[55] Thompson, D., 1993. "Wheel-rail noise generation, part v: Inclusion of wheel rotation". *Journal of Sound and Vibration,* **161**(3), pp. 467 – 482. → pages 22, 72

[56] Thompson, D., 2009. *Railway Noise and Vibration*. Elsevier, Oxford. → pages 23

[57] Rudd, M., 1976. "Wheel/rail noise–part ii: Wheel squeal". *Journal of Sound and Vibration,* **46**(3), pp. 381 – 394. → pages 23, 24

[58] Heckl, M., and Abrahams, I., 2000. “Curve squeal of train wheels, part 1: Mathematical model for its generation”. *Journal of Sound and Vibration,* **229**(3), pp. 669 – 693. → pages 24

[59] Heckl, M., 2000. “Curve squeal of train wheels, part 2: Which wheel modes are prone to squeal?”. *Journal of Sound and Vibration,* **229**(3), pp. 695 – 707. → pages 24

[60] Heckl, M., and Huang, X. Y., 2000. “Curve squeal of train wheels, part 3: Active control”. *Journal of Sound and Vibration,* **229**(3), pp. 709 – 735. → pages 24

[61] Schneider, E., Popp, K., and Irretier, H., 1988. “Noise generation in railway wheels due to rail-wheel contact forces”. *Journal of Sound and Vibration,* **120**(2), pp. 227 – 244. → pages 24

[62] Fingberg, U., 1990. “A model of wheel-rail squealing noise””. *Journal of Sound and Vibration,* **143**(3), pp. 365 – 377. → pages 24

[63] van Ruiten, C., 1988. “Mechanism of squeal noise generated by trams”. *Journal of Sound and Vibration,* **120**(2), pp. 245 – 253. → pages 24

[64] Airey, J. R., 1910. “The vibrations of circular plates and their relation to bessel functions”. *Proceedings of the Physical Society of London,* **23**(1), p. 225. → pages 24

[65] Lamb, H., and Southwell, R. V., 1921. “The vibrations of a spinning disk”. *Proceedings of the Royal Society of London. Series A, Containing Papers of a Mathematical and Physical Character,* **99**(699), pp. pp. 272–280. → pages 25

[66] Southwell, R., 1922. “On the free transverse vibrations of a uniform circular disc clamped at its centre; and on the effects of rotation”. *Proceedings of the Royal Society of London. Series A, Containing Papers of a Mathematical and Physical Character,* **101**, pp. 133–153. → pages 25

[67] Bhuta, P., and Jones, J., 1963. “Symmetric planar vibrations of a rotating disk”. *Journal of the Acoustical Society of America,* **35**, pp. 982–989. → pages 25

[68] Chen, J., and Jhu, J., 1996. “On the in-plane vibration and stability of a spinning annular disk”. *Journal of Sound and Vibration,* **195**(4), pp. 585 – 593. → pages 25

[69] Deshpande, M., and Mote Jr., C. D., 2003. "In-plane vibrations of a thin rotating disk". *Journal of Vibration and Acoustics,* **125**(1), pp. 68–72. → pages 25

[70] Baddour, N., and Zu, J. W., 2001. "A revisit of spinning disk models. part i: derivation of equations of motion". *Applied Mathematical Modelling,* **25**(7), pp. 541 – 559. → pages 25

[71] Baddour, N., and Zu, J. W., 2001. "A revisit of spinning disk models. part ii: linear transverse vibrations". *Applied Mathematical Modelling,* **25**(7), pp. 561 – 578. → pages 25

[72] Hutton, S., Chonan, S., and Lehmann, B., 1987. "Dynamic response of a guided circular saw". *Journal of Sound and Vibration,* **112**(3), pp. 527 – 539. → pages 25

[73] Hutton, S., 1991. "The dynamics of circular saw blades". *European Journal of Wood and Wood Products,* **49**, pp. 105–110. 10.1007/BF02614349. → pages 25

[74] Tobias, S., and Arnold, R. N., 1957. "The influence of dynamical imperfection on the vibration of rotating disks". *ARCHIVE: Proceedings of the Institution of Mechanical Engineers 1847-1982 (vols 1-196),* **171**, pp. 669–690. → pages 25, 27

[75] Dorf, R. C., and Bishop, R. H. *Modern Control Systems*. Prentice Hall. → pages 37, 41

[76] Goldstein, H., 1950. *Classical mechanics*. Addison Wesley. → pages 73